2013

Computational Modeling of Graphene Oxide Exfoliation and Lithium Storage Characteristics

Reza Mortezaee
Wright State University

Computational Modeling of Graphene Oxide Exfoliation and Lithium Storage Characteristics

A thesis submitted in partial fulfillment

of the requirements for the degree of

Master of Science in Engineering

By

Reza Mortezaee

B.S. (1997) and M.S. (1999) in Electrical Engineering,

Sharif University of Technology

2013

Wright State University

WRIGHT STATE UNIVERSITY

GRADUATE SCHOOL

May 24, 2013

I HEREBY RECOMMEND THAT THE THESIS PREPARED UNDER MY SUPERVISION BY Reza Mortezaee ENTITLED Computational Modeling of Graphene Oxide Exfoliation and Lithium Storage Characteristics BE ACCEPTED IN PARTIAL FULFILLMENT OF THE REQUIREMENTS FOR THE DEGREE OF Master of Science in Engineering.

Amir Farajian, Ph.D.

Thesis Director

George Huang, Ph.D., Chair
Department of Mechanical and Materials Engineering

Committee on Final Examination

Hong Huang, Ph.D

James Menart, Ph.D

R. William Ayres, Ph.D.
Interim Dean, Graduate School

ABSTRACT

Reza Mortezaee, M.S.Egr., Department of Mechanical and Materials Engineering, Wright State University, 2012. Computational Modeling of Graphene Oxide Exfoliation and Lithium Storage Characteristics

Graphene oxide is a two dimensional material obtained by adsorption of oxygen or oxygen-containing groups on graphene. Stacked layers of graphene oxide constitute graphite oxide. These materials have various applications such as a source material for graphene production, transport support for electron microscopy, flexible organic photovoltaic cells and use in Li-ion batteries. Generation of exfoliated graphene oxide from a graphite oxide precursor is achieved relatively easily in solution as compared to graphene exfoliation. In this study we investigate the details of the graphene oxide exfoliation procedure in solution by calculating the Gibb's free energies and reaction rates. We consider two surface coverages, 50% and 100%, and two adsorption groups; epoxy and hydroxyl groups. The interlayer interactions and stable configurations are calculated using the local density approximation in density functional theory for periodic structures, and molecular mechanics based on universal force field for nanosheets. Our results show that exfoliation of graphene oxide in water happens through intercalation of water molecules between the layers and not through the slide of layers without water intercalation. The feasibility of the former mechanism arises from the stabilization effect of hydrogen bonds as compared to the destabilization effect of increased interlayer distance.

We also assess some of the characteristics of graphene oxide materials relevant to applications in renewable and clean energy fields. These characteristics include electronic band structure and lithium storage properties.

TABLE OF CONTENTS

LIST OF FIGURES

LIST OF TABLES

ACKNOWLEDGEMENTS

Most importantly, I would like to acknowledge Dr. Amir Farajian for his tireless efforts in guiding me through this research project. His passion and enthusiasm for this work has instilled in me a great desire to achieve success in all I do. His unwavering support has been an integral part in my achievements thus far, and I am very fortunate to have had the opportunity to work with him on this thesis.

A special thanks to committee members Dr. Hong Huang and Dr. James Menart for their time and support during the final defense stages. I would also like to express my appreciation for the work of Dr. James Menart in creating such a relevant and challenging renewable and clean energy degree program.

I am also grateful to my fellow students Kirti K. Paulla and Tim H. Osborn, two Ph.D. candidates who helped me a lot in doing this research project.

This research was supported by the National Science Foundation Grants ECCS-0925939 and STTR Phase II grant IIP-1057999, and by Department of Energy Renewable and Clean Energy Education Initiative Agency/Sponsor No: AGRMT RSC11006 ACCT 4496010001.

DEDICATION

This dissertation is lovingly dedicated to my mother whose support, encouragement and constant love have sustained me throughout my life.

1. INTRODUCTION

Graphene, a recently discovered two-dimensional honeycomb carbon lattice, has emerged as a novel material and received much attention over the past few years for its excellent thermal, electrical and optical properties. Despite the novelty of graphene, the discovery graphene oxide dates back to one century and half ago when the chemistry of graphite was investigated by testing its reactivity. As a result of one of those tests, B. C. Brodie, a British chemist, discovered the ability of oxidizing graphite when he came across a product material composed of carbon, oxygen and hydrogen with an increased overall mass compared to the initial graphite. It was about one century later when Boehm et al. [1] concluded that some of these graphite oxide platelets were actually as thin as a one layer carbon sheet. Nowadays, the existence of graphite oxide monolayers is a widely accepted fact and is usually referred to as graphene oxide [2], [3]. Every sheet of graphene oxide can be described as the graphene with oxygen functional groups on both sides of the plane and around the edges [4], [5].

1.1 Structure of Graphene Oxide

Exact structure of graphene oxide has been the subject of much debate over the past few decades and there is still no unique commonly accepted model for it [6] and it will probably remain so in the future. The main reason for this ambiguity is that graphene oxide is amorphous and what is found in reality is different from one sample to another depending on the type of synthesis used for its production and the degree of oxidation. The layer structure of graphene is similar to its parent graphite but it is not as flat and

buckles to some extent as it is seen in Fig. 1. “Oxide” does not mean it only has oxygen; it also has other functional groups and packing of its layers (in case it is more than one sheet) is rather disordered and irregular. Therefore, graphene oxide is really a non-stoichiometric compound where the relative number of atoms cannot be represented by a ratio of integer numbers. It typically consists of different randomly positioned functional groups and up to this date there is no analytical method to precisely model these types of structures. This is why computational nanomaterial researchers have no choice but to settle for the lattice based periodic models of graphene oxide.

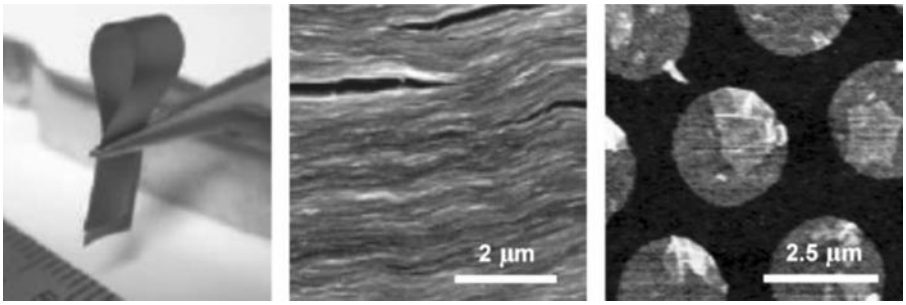

Figure 1: Left image shows a graphene oxide paper ribbon [7]. Picture in the middle shows an edge view of graphene oxide paper [7]. The right image shows a photograph of the same sheets attached to an amine-terminated template on a gold surface [8].

Therefore due to the above-mentioned reasons, instead of one model, there are several proposed chemical structures for graphene oxide. Nevertheless, it can generally be assumed that the structure of graphene oxide is a graphene sheet bonded to oxygen in the form of epoxide species (C=O), hydroxyl (C-OH), carboxyl (COOH), epoxide (C-O-C) and other C=O or C-O containing chemical species. The ratio of the number of carbon atoms to oxygen atoms is about 2 [9]. Graphite oxide has very low electrical conductivity

and it usually does not have a long range sp^2 structure and is mainly a mixture of sp^2 and sp^3 hybridized carbons [9]. A number of mainstream graphene oxide models used in the literature are introduced here in a chronological order.

The Hofmann structure (Fig. 2) is one of the earliest structure models proposed for graphene oxide. It consists of functional groups including an oxygen atom joined by single bonds to two adjacent carbon atoms. These oxygen functional groups are spread all over the basal planes of graphite so that graphene oxide in this model has a chemical formula of C_2O.

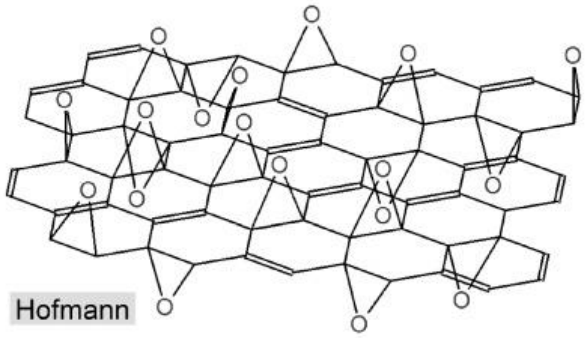

Figure 2: Hofmann structure for graphene oxide [10].

The Ruess structure (Fig. 3) is a modified version of the Hofmann structure to take hydrogen content of graphene oxide into account. This is done by adding another chemical functional group to the basal planes. These functional groups contain an oxygen atom connected to a hydrogen atom by a covalent bond (hydroxyl groups). As it seen

from Fig. 3, the basal plane structure in the Ruess model does not have the sp^2 hybridized system of the Hofmann model and changes it into the sp^3 hybridized system.

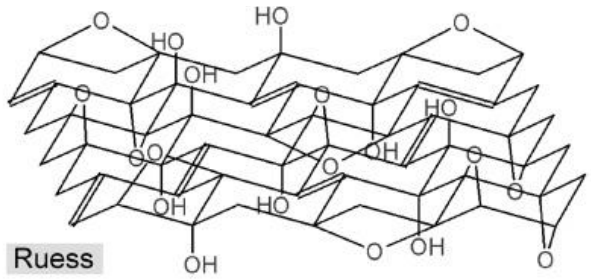

Figure 3: Ruess structure for graphene oxide [10].

In the Scholz-Boehm structure (Fig. 4), the epoxide and ether groups are removed. It has regular quinoidal species in a corrugated backbone. The Nakajima-Matsuo model (Fig. 5) is another proposed model of graphene oxide that like the other 3 models introduced so far is formed by repeat units.

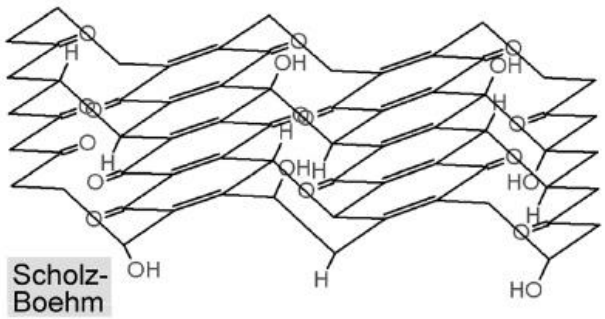

Figure 4: Scholz-Boehm structure for graphene oxide [10].

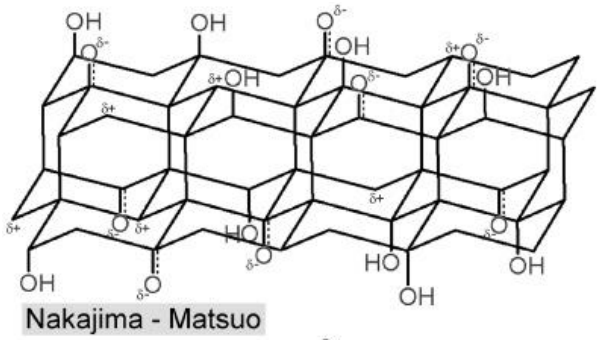

Figure 5: Nakajima-Matsuo structure for graphene oxide [10].

The Lerf-Klinowski structure (Fig. 6) is the most recent proposed structure. It assumes graphene oxide is amorphous and non-stoichiometric and therefore is the only structure of graphene oxide introduced here that is not based on a lattice (that is formed by repeat units). This structure is the first one that was proposed using observations based on solid state nuclear (NMR) spectroscopy [11], while the first four models were based on other techniques like X ray diffraction, reactivity and elemental composition.

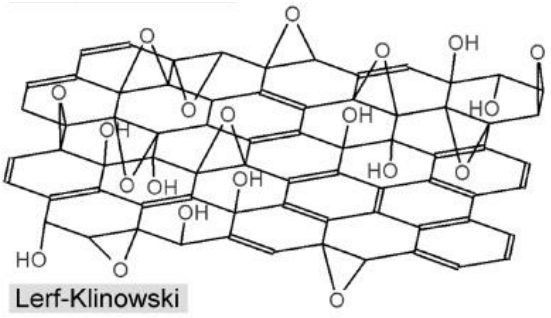

Figure 6**:** Lerf-Klinowski structure for graphene oxide [10].

1.2 Applications of Graphene Oxide

In this section, several applications of graphene oxide are introduced. Other than its use for production of graphene, other applications mentioned here have been used or proposed using more recent experimental observations.

1.2.1 Source Material for Production of Graphene

Discovery of graphene has been followed by the question of how graphene can be manufactured in a large scale and cost-effective way. On the other hand, graphene oxide reduction results in a material similar to graphene (to varying degrees) and sometimes it is very close to pristine graphene. This resemblance to graphene has made graphene oxide reduction one of the most important chemical reactions of it and at the same time one of its most common applications. Nowadays, for researchers and those who want to use graphene in large scale energy storage applications, reduction of graphene oxide is the first priority in manufacturing graphene-like materials. Once mass production of graphene is achieved by graphene oxide reduction, produced graphene can be used in applications like sensors, energy materials and clean energy devices, among many others.

1.2.2 Transparent Support for Electron Microscopy

This application was proposed when the structure of graphene oxide (GO) was analyzed by transmission electron microscopy (TEM) [12]. According to the results based on electron diffraction, the underlying carbon lattice maintains the order and lattice spacing

of graphene on average. In fact, it was shown that the interatomic spacing in graphene oxide is only, at most, half a percent different than graphene. Atomically resolved images of graphene oxide show that it has the same lattice substrate as graphene. It means single graphene oxide sheets are highly electron transparent, like graphene, because of their low atomic number and 2 dimensional structures. Therefore they could be used as films to support nanoparticles and macromolecules in TEM structural analyses. What makes using graphene oxide a better choice than graphene is the difficulty of manufacturing graphene, especially in the size and geometry needed for TEM support applications, while graphene oxide is easy and inexpensive to fabricate in any laboratory. Another advantage of graphene oxide is its stability under electron beam bombardment, resulting in low background in both diffraction and imaging modes.

1.2.3 Doping Application for Supercapacitor Materials

Graphene oxide is also suggested for doping polyaniline to be used in supercapacitors [13]. In this application graphene oxide sheets were used for doping fibrillar polyaniline (PANI) nanofibers resulting in a high performance novel electrode material. The produced nanocomposite, with the mass ratio of graphene oxide/aniline 1:100, has an electrical conductivity of 10 $\left(\frac{S}{cm}\right)$ at a temperature of 295 °K. It has a specific capacity of 531 $\left(\frac{F}{g}\right)$ which is nearly 2.5 times bigger than the original individual PANI. Doping and the ratio of applied graphene oxide have a strong effect on the specific capacity of the nanocomposite product.

1.2.4 Medical Diagnostics and Biotechnology

Graphene oxide is now getting application in medical diagnostics and biotechnology. Carboxyl-modified graphene oxide (GO-COOH) has been reported to have the ability of detecting glucose in diluted blood, buffer solution or fruit juice samples [14] due to its ability to produce a blue color reaction in the presence of hydrogen peroxide (H_2O_2) and peroxidase substrate tetramethylbenzidine (TMB).

According to intrinsic peroxidase property of this type of graphene oxide, a colorimetric method for detection of H_2O_2 and glucose was proposed by using the GOCOOH-catalyzed blue color reaction. The catalytic activity of GOCOOH depends on concentration of hydrogen peroxide, so it can be used for detection of H_2O_2. On the other hand, the main product of glucose oxidase catalyzed reaction is H_2O_2. So GOCOOH can be used for detection of glucose instead of traditionally used horseradish peroxidase (HRP). Compared to HRP, GOCOOH is cheap, easy to manufacture and more stable.

1.2.5 Flexible Organic Photovoltaic Cells

In cutting edge flexible and transparent electronic applications like photovoltaics or e-papers, materials with high optical transparency, electrical conductivity, mechanical robustness under bending and the ability of low-cost and large-area production are needed [15]. Indium tin oxide (ITO) is only conductive and transparent but not flexible, so its applicability is limited to rigid optoelectronic devices [16]. So for flexible applications an alternative material is demanded.

Ten years ago the fact that a one sheet carbon structure (graphene) is stable under room and high temperatures was discovered. Graphene nearly has all the requirements of being used as a substitution of ITO in flexible optoelectronics [17-19]. In the past few years several groups have proved experimentally the ability of some graphene-based materials to be used in organic photovoltaics [20-23]. But, most of the graphene oxide reduction methods [24-27] have failed to be compatible with flexible substrates of graphene like polyethylene terephthalate (PET), because PET melts at the high temperatures needed for the reduction process. Recently a method of graphene oxide reduction has been developed [28-32] that does not need high temperature annealing so that at the end of the reduction process, the PET substrate remains intact. This method uses laser irradiation for reduction of spin-coated graphene oxide films on PET substrates (Fig. 7) [28]. Another advantage of this method is that it does not need as much time as required by methods that use chemical or high temperatures for reduction of graphene oxide and shortens it from several hours to a few minutes [28, 33]. During the process, the O:C ratio decreases from 61 to 17% [28]. The produced LrGO can be used and integrated in polymer-fullerene photovoltaic cell as the transparent electrode. For a high efficiency in this application, the electrode film should be as conductive and transparent as possible. Therefore, a tradeoff between these two properties is inevitable.

1.2.6 Use in Li-ion Batteries

Although graphite has been widely used as an anode material in Li-ion batteries, the energy density is not enough for some applications. Use of some transition metal oxides

such as Fe_2O_3, Co_3O_4, MoO_3 and Fe_3O_4 instead of graphite yields larger reversible capacity than graphite. However, during each cycle of charging and discharging, transition metal oxides break into small metal clusters as a result of their reaction with Li and form Li_2O. It causes a loss of capacity during each cycle especially at high rates [34, 35].

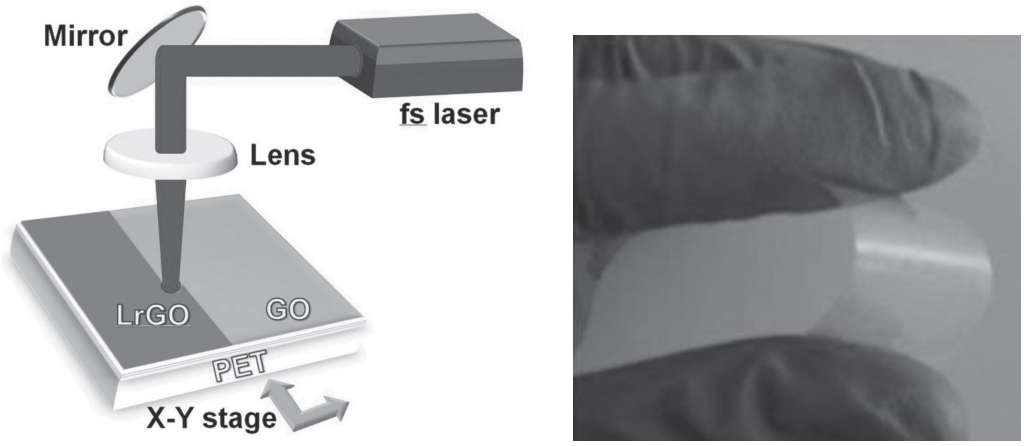

Figure 7: Left schematic picture shows arrangement used for reduction of graphene oxide films on a PET substrate. Fs laser and LrGO stand for femtosecond laser beam and laser-reduced graphene oxide respectively. The right picture shows the reduced graphene oxide after pulsed-laser photoreduction process [28].

For this reason, "nanostructured" metal oxides have been used to increase the capacity, which might be a result of their shortened Li^+ insertion-extraction pathways [34], [36]. Due to high electronic conductivity of different chemically modified graphene materials, they have been added to metal oxide particles like TiO_2, SnO_2 and Mn_3O_4 to increase the conductivity [37]. These hybrid materials are then used in Li-ion batteries to increase electrode capacity and cycling stability [38], [39].

Composites including reduced graphene oxide platelet and metal oxide nanoparticles are among those hybrid materials that are proposed as electrodes for Li-ion batteries. For example, a composite of reduced graphene oxide platelets and Fe_2O_3 nanoparticle has been reported [40]. Fe_2O_3 nanoparticles are uniformly distributed on the surface of the reduced graphene oxide platelets. This composite has about 1700 and 1230 (mAh/g) first charge and discharge capacity respectively at a current density of 100 (mAh/g). Specific capacity of this composite is more than the sum of reduced graphene oxide and Fe_2O_3 nanoparticles, showing a desirable synergistic effect of the two constituent materials of the composite that is beneficial to its overall electrochemical performance. Besides, this composite exhibits good cycle life.

1.3 Manufacturing of Graphene Oxide

Fig. 8 shows a schematic representation of the procedure used to manufacture graphene oxide [41]. Nearly all methods of manufacturing graphene oxide start with oxidization of graphite [42]. Flake graphite, which is the most common variety of naturally found graphite, is usually used for chemical reactions of graphite including its oxidation [43]. π-structure of flake graphite has many localized defects as a result of its natural origin. These defects serve as seed points for its oxidization process. On the other hand, these defects make flake graphite's structure more complex and therefore clarification of its exact oxidization mechanisms difficult [42].

Typically graphite is oxidized by one of the Brodie, Staudenmaier or Hummers methods. In the first two methods a combination of nitric acid (HNO_3) and potassium chlorate

($KCLO_3$) is used for oxidization of graphite, but Hummers method involves reaction of sulfuric acid (H_2SO_4) and potassium permanganate ($KMnO_4$) with graphite. Graphite oxide contains lots of oxygen-containing functional groups which make it a good choice for using in a broad range of applications. Placement of these functional groups on both sides of graphene oxide sheets overcomes weak van der Waals forces between adjacent layers and extends the interlayer spacing. So, as it is shown schematically in Fig. 8, oxidation of graphite to graphite oxide results in an increased distance between neighboring layers. The sheets in such an extended structure can be easily pulled apart by applying an external force.

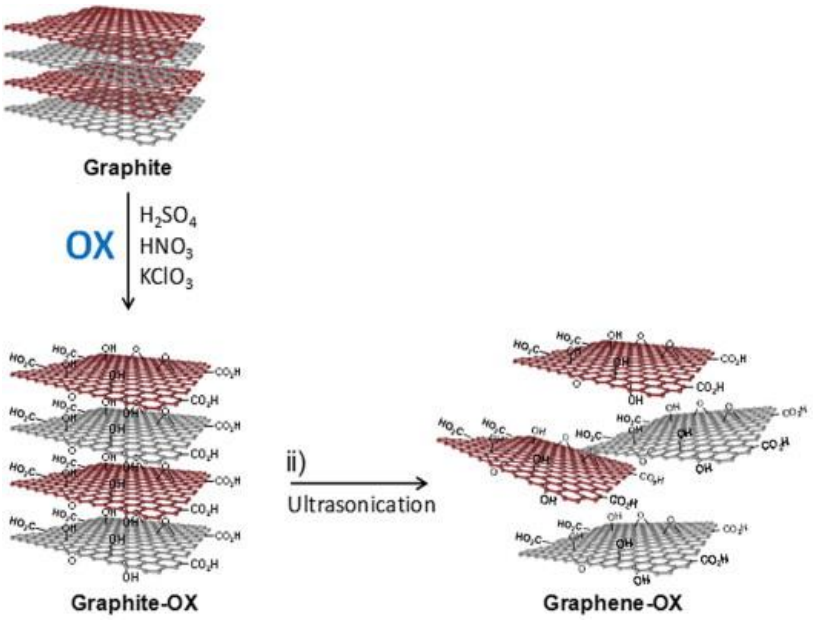

Figure 8: Schematic of the procedure for synthesis of graphene oxide using graphite as the starting material. Using an oxidative treatment, the initial graphite is converted to graphite oxide. At the end, graphene oxide is produced using exfoliation of graphite oxide [44].

Accordingly, the next step is exfoliation of the produced graphite oxide into individual graphene oxide sheets. Many solvents can be used for this purpose. Graphite oxide also disperses very well in water [45]. Exfoliation of graphene oxide platelets into individual sheets can be facilitated by rapid heating [46], [47], stirring the mixture of graphite oxide and water for a long enough time or more commonly by using sound (usually ultrasound) energy for making agitation (sonication) [42]. By applying ultrasonication on graphite oxide in water or different organic solvents, the hydrogen bonds between the neighboring graphene oxide sheets can be cut, resulting in a stable dispersion of graphene oxide [48]. Atomic force microscopy of graphene oxide platelets shows ultrasonication leads to nearly full exfoliation of graphite oxide [49]. Although ultrasonication of graphite oxide in water or other solvents is a faster method than stirring, it causes damage to the platelets of graphene oxide while with the stirring method they remain intact [50].

The main difference between graphite oxide and its exfoliated graphene oxide sheets is the surface area, which is higher for graphene oxide. Other than different surface areas, there is no major difference between them. Even their electronic structures and properties are similar (this is not the case for graphene and graphite).

Using the above-mentioned method, the graphite oxide is exfoliated into multi-layered (platelets) or even single-layered (sheets) of graphene oxide. Produced graphene oxide has multiple defects and the number of defects is dependent on the amount of oxidant used for oxidization of graphite and the oxidizing time. Here “platelet” refers to a thick multilayer of graphene oxide, and “sheet” means a monolayer to few layers of the material.

The thickness of a single layer graphene oxide sheet (1-1.4 nm) is more than the thickness of an ideal monolayer of graphene itself (~ 0.34 nm). This is due to the presence of oxygen functional groups and absorbed molecules on both sides of the graphene oxide plates [2], [51]. The presence of oxygen functional groups has another effect on graphene oxide. They make graphene oxide hydrophilic (unlike graphene that is hydrophobic) due to strong interactions between water and these functionalities so that water easily intercalates between the sheets and disperses them. This is why graphite oxide is easily dispersed in water. This also causes multilayered graphene oxide to have trapped H_2O molecules between the layers [4], [51], [52]. Using thermal reduction the number of these trapped water molecules can be reduced if needed, [51], [53] but removing all water molecules from the structure might be difficult because heating at 60–80 °C causes partial decomposition and degradation of graphene oxide.

1.4 Bandgap of Graphene Oxide

The bandgap of pristine graphene is zero and it is considered a semi-metal. Oxygen functionalization of graphene causes the bandgap of graphene to open as it can be seen from Fig. 9. Bandgap increases monotonically with level of oxygen coverage at higher coverage but the dependence is not clear at lower coverage as some local up and down can be seen in the figure [54], [55]. At higher ratios of oxygen to carbon numbers like 25% [56], the band gap starts increasing continuously. The graphene oxide structures used for band gap calculations in Fig. 9 have oxygen atoms on the bridge sites. Oxygen

atoms are located only on one side of the graphene layer while the other side is put on substrate.

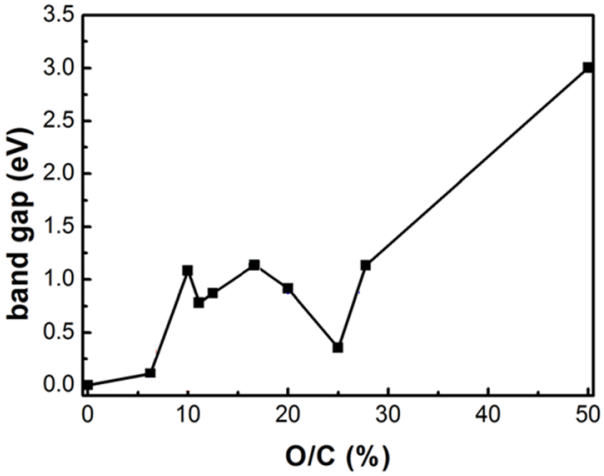

Figure 9: Variation of the band gap versus oxygen coverage of graphene oxide [56]

There is another thing that differs significantly for low and high oxygen coverage. The effect of lattice relaxation on the band gap also changes for low and high oxygen coverage. In low oxygen coverage, lattice relaxation does not have a big effect on the calculated band gap of graphene oxide, but at higher coverage it changes the band gap significantly [56].

2. METHOD

Nearly all physical properties and structures of materials are dependent on total energies or differences between total energies. For example defects and surfaces in a solid material are decided in a way to minimize the total energy. Therefore by calculating total energies, properties that are related to total energy or to a difference between total energies can be predicted.

Quantum mechanics theory is the only one among comparable paradigms (such as Newtonian mechanics and special relativity) that is able to calculate total energy of a system of nuclei and electrons in good accordance with experimental observations. Using quantum mechanics, the total energy of a one-atom system has been predicted very accurately. The rules for calculating energies of larger systems are simply extension of the smallest one, except their computational methods require some approximation, producing less accurate results compared to experiments. Nowadays, using quantum mechanics of electrons and ions, most of low-energy chemistry and physics can be explained. For instance, the total energy technique has been successfully used to predict phase transition temperatures and pressures, lattice constants, bulk moduli, among many others. Quantum theory has also been successful in explaining phenomena such as energy levels of atoms, covalent bonds and the distinction between a metal and insulator [57].

If performing experiments was always possible and low cost, there would not be a need for quantum mechanical calculations. But providing experiment facilities is not always possible or at low cost. This makes using quantum mechanics sometimes necessary to predict physical properties of materials. This is not to say that for large systems composed of many electrons and nuclei (many-body systems) quantum mechanical

computations are not without cost. In fact, a disadvantage of methods using quantum mechanics is their computational cost as it often needs enormous amounts of CPU time, memory and disk space even for unit cells composed of only a few atoms. Time needed to complete computations increases exponentially with the number of atoms in the structure. Therefore, total energy calculations using quantum mechanics can be done only when some approximations are introduced into the method, but in an appropriate way so that changes in the final results are within acceptable tolerances.

2.1 Born-Oppenheimer Approximation

This approximation was proposed by Max Born and J. Robert Oppenheimer in 1927 shortly after the introduction of quantum mechanics. It is based on the huge difference between masses of electrons and nuclei in a molecule and at the same time little difference between coulomb forces exerted on them. This approximation leads to a separation of nuclear and electronic coordinates. To have a better understanding of this approximation, assume a molecule has n nuclei and m electrons. Without the Born–Oppenheimer approximation, for solving the time independent Schrödinger equation a partial differential of $3 \times (n + m)$ variables should be solved. This is the total number of spatial coordinates of nuclei and electrons. But using the approximation, the wave function can be considered as multiplication of two nuclear and electronic contributions:

$$\Psi_{total} = \Psi_{nuclear} \times \Psi_{electronic} \tag{2-1}$$

First, the electronic contribution to the wave function, which is dependent only on electrons, is determined using a partial differential equation of 3n variables while the

nuclei are kept fixed. Then the nuclear contribution to the wave function is determined using a partial differential equation of 3m variables while the electronic wave function obtained in the first step serves as the potential energy of the Schrödinger equation.

Even with the Born–Oppenheimer approximation, solving Schrödinger equation for large systems is still very difficult. The most difficult part is how to calculate the electron-electron interactions. Since electrons are fermions, the wave function of a many-electron system is antisymmetric. This antisymmetry causes electrons with the same spin to have spatial separation which in turn reduces the coulomb energy of the system [57]. The level of reduction is referred to as exchange energy. There is no difficulty considering exchange energy in total energy calculations (Hartree-Fock), but there is still another reduction in total energy to be taken into account.

More reduction in coulomb energy, and hence many-body energy of the system, is realized by considering the fact that electrons with opposite spins are also spatially separated [57]. The amount of reduction is named correlation energy. Calculating correlation energy for a system of many electrons is very difficult.

This is why it was mentioned earlier that even after introducing the Born–Oppenheimer approximation, the total energy calculation for a system of many electrons is still difficult. Therefore, there is still a need for other simplifications to deal with electron-electron interactions.

2.2 Density Functional Theory

Density functional theory (DFT) is a modeling method based on quantum mechanics used to address the problem of dealing with electron-electron interactions in many-electron systems. This theory is an exact theory [58], but as discussed later, some terms related to exchange and correlation energies in its equations are difficult to know exactly. Therefore, an approximation for calculating those energies is needed. DFT was first proposed by Hohenberg and Kohn [59] and developed further by Kohn and Sham [60] in the mid-1960s. This theory, in principle, deals with electron-electron interactions in that it allows converting the problem of an interacting electron gas in the presence of nuclei to the problem of movement of a single electron in an equivalent non-local potential. Interestingly, local approximation to this non-local potential is still accurate despite the fact that the nonlocal potential is not known precisely. It is shown [60] that a set of self-consistent and single-electron equations can exactly describe a many-electron system. Total energy calculation using density functional theory has predicted ground state properties accurately. The word "functional" in the theory's name is used because in this theory a set of functions is mapped to a set of numbers in contrast to a "function" that is used to map a set of numbers to another set of numbers [58]. After doing many calculations using this theory and comparing results with experiments, it is now generally believed that total energies calculated using this method will be within a few percent of the actual ones and structural parameters within 0.1 Å of the real distances, but difference in cohesive energies may be more than ten percent.

$E[\{\Psi_i\}]$ in the following equation is the Kohn-Sham energy functional of a set of doubly occupied energy states (Ψ_i):

$$E[\{\Psi_i\}] = 2\sum_i \int \Psi_i \left[-\frac{\hbar^2}{2m}\right] \nabla^2 \Psi_i d^3r + \int V_{ion}(r) n(r) d^3r + \frac{e^2}{2} \int \frac{n(r)n(r')}{|r-r'|} d^3r d^3r' +$$

$$E_{XC}[n(r)] + E_{ion}(\{R_I\}) \qquad (2\text{-}2)$$

where,

E_{ion} : Coulomb energy of mutual effects between the nuclei at positions $\{R_I\}$

V_{ion} : Total static ion-electron potential

$E_{XC}[n(r)]$: Exchange-correlation energy functional

$n(r)$: Electronic density calculated by the following relation:

$$n(r) = 2\sum_i |\Psi_i(r)|^2 \qquad (2-3)$$

Only at its minimum, the Kohn-Sham energy functional has a physical meaning where it represents the ground state energy of a system of electrons with the nuclei at positions $\{R_I\}$. Therefore, the set of wave functions (Ψ_i) minimizing the energy functional must be determined by solving the Kohn-Sham equations:

$$\left[-\frac{\hbar^2}{2m}\nabla^2 + V_{ion}(r) + V_H(r) + V_{XC}(r)\right]\Psi_i(r) = \varepsilon_i \Psi_i(r) \qquad (2-4)$$

where,

Ψ_i : Wave function of the ith electronic state

ε_i : Kohn-Sham eigenvalue

V_H : Hartree potential of the electrons calculated by the following equation,

$$V_H(r) = e^2 \int \frac{n(r')}{|r - r'|} d^3r' \qquad (2-5)$$

V_{XC} : Exchange-correlation potential calculated using the following relation:

$$V_{XC}(r) = \frac{\delta E_{XC}[n(r)]}{\delta n(r)} \qquad (2-6)$$

The Kohn-Sham equations are advantageous in that they convert a system of many interacting electrons to a system of non-interacting electrons in which each electron moves in an equivalent potential representing the effect of other electrons.

As the apparent form of equation 2-4 suggests, the Kohn-Sham equations can be considered as eigenequations and the terms inside brackets as the Hamiltonian. However, eigenvalues of these equations are not energies of the single-particle electron states. Therefore, their sum does not give the total electronic energy because it considers some electron-electron effects like exchange energy twice; one in the Hartree energy and the other one in exchange-correlation energy. Instead, Kohn-sham eigenvectors are derivatives of the total energy with respect to the occupation number of these states [57].

2.3 Local Density and Generalized Gradient Approximations

For solving Kohn-Sham equations, exchange and correlation energy functionals must be known, but as it was mentioned earlier it is not possible to know them exactly in a many-electron system. Therefore, an approximation is needed to express exchange-correlation energy as a function of electron density. The most commonly used method in pseudopotential total energy calculations is the local density approximation (LDA) [60].

This approximation comes from the assumption that the exchange-correlation energy per electron in an electron gas at point r, $\varepsilon_{XC}(r)$, is the same as exchange-correlation energy per electron in a homogenous electron gas with a uniform density the same as the electron gas density at point r. In other words, LDA ignores the effect of nearby inhomogeneities in the electron density on exchange-correlation energy [57]. This assumption yields the following relations:

$$\varepsilon_{XC}(r) = \varepsilon_{XC}^{hom}[n(r)] \qquad (2-7)$$

$$E_{XC}[n(r)] = \int \varepsilon_{XC}(r)n(r)d^3r \qquad (2-8)$$

Results of computations that use local density approximation have been well in accordance with experimental data for some applications [57].

Since LDA results are not accurate where there are rapid changes in electron density, such as in molecules, there are a few other methods for approximating exchange-correlation functionals such as generalized gradient approximation (GGA) [61]. The GGA method has good results for molecular geometries and ground-state energies. This method is still local but at the same time considers the gradient of the density at the same coordinate in the following relation:

$$E_{XC}[n(r)] = \int \varepsilon_{XC}(r, \nabla n)n(r)d^3r \qquad (2-9)$$

2.4 Pseudopotential Approximation

Pseudopotential theory is another approximation used to make many-body problems simpler to solve [57]. In solids, physical properties are much more dependent on the valence electrons than on non-valence electrons. This fact is used by the pseudopotential or equivalent potential approximation. This theory was introduced first by Hans Hellmann in the mid-1930s. It is used to model the complicated effects of the motion of non-valence (core) electrons and the nucleus of an atom with an equivalent potential or pseudopotential. Using this approximation, the columbic potential of non-valence electrons in Schrödinger equation is replaced by an equivalent potential. Using the pseudopotential approximation, the valence wave function is orthogonal to all the core wave functions which is a requirement of the exclusion principle.

In the Fig. 10, the potential energy by considering all non-valence electrons and its pseudopotential approximation are schematically depicted. Their corresponding wave functions are also shown in the picture. As it can be seen from the picture, r_c is the radius at which model including all electrons and its pseudopotential approximation start to have the same result.

2.5 Universal Force Field (UFF)

A force field based on Newtonian physics is used in Molecular Mechanics (MM) to predict molecular equilibrium structures. A force field specifies the type of mathematical functions and values of the parameters used in those functions to describe the potential energy of a system of molecules and atoms. Universal force field (UFF) was developed to

overcome the common problem of previous popular force fields whose applications were limited to specific combinations of atoms.

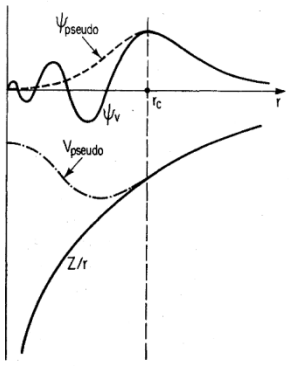

Figure 10: Schematic potential energy by considering all non-valence electrons and its pseudopotential approximation along with their corresponding wave function [57].

Using UFF, different atomic associations across the periodic table can be studied. UFF provides a force field using general rules and atomic parameters. This force field is capable of predicting bond distances with errors less than 0.1 Å and angle bends with errors less than 5° to 10° [62]. Parameters used to generate the UFF are based only on the element, its connectivity and hybridization. These parameters include atomic bond radii which depend on hybridization, hybridization angles, van der Waals parameters, torsional and inversion barriers and effective nuclear charges. UFF is able to consider these different geometries [62]: linear, trigonal, resonant, tetrahedral, square planar, trigonal bipyramidal and octahedral. In UFF, potential energy of a molecule with an arbitrary geometry is sum of valence or bonded interactions and non-bonded interactions [62]:

$$E = E_R + E_\theta + E_\varphi + E_\omega + E_{vdw} + E_{el} \qquad (2-10)$$

Bonded interactions include bond stretching (E_R) and angular distortions. Angular distortions consist of bond angle bending (E_θ), dihedral angle torsion (E_φ) and out-of-plane or inversion (E_ω). Included as non-bonded interactions are van der Waals (E_{vdw}) and electronic potential (E_{el}). The above relation can also be written explicitly in the following form [58]:

$$\begin{aligned} U = & \sum_{bonds} \frac{1}{2} k_{AB}(R_{AB} - R_{e,AB})^2 + \sum_{bends} \frac{1}{2} k_{ABC}(\theta_{ABC} - \theta_{e,ABC})^2 \\ & + \sum_{bends} \frac{U_0}{2}\left(1 - \cos\left(n(\chi - \chi_0)\right)\right) \\ & + \sum_{out-of-plane} \frac{k}{2\,sin^2\psi_e}(\cos\psi - \cos\psi_e)^2 + \sum_{nonbonded} \left(\frac{C_{AB}^{12}}{R_{AB}^{12}} - \frac{C_{AB}^{6}}{R_{AB}^{6}}\right) \\ & + \frac{1}{4\pi\varepsilon_0} \sum_{charges} \frac{Q_A Q_B}{R_{AB}} \end{aligned} \qquad (2-11)$$

where,

K_{AB} = force constant,

R_{AB} = instantaneous bond length

$R_{e,AB}$ = equilibrium bond length

χ = ABCD angle

n = periodicity number

Q = atomic charge

2.6 Exfoliation Rate Calculation

Earlier in section 1.3, a few methods for exfoliating bulk graphite oxide into graphene oxide sheets such as ultrasonification, rapid heating and agitation were discussed. Exfoliation rate is defined as the number of graphene oxide sheets that are exfoliated per unit of time. The following formula is used to calculate the exfoliation rate of graphene oxide sheets (relation 28.72 in [63]):

$$R = \frac{k_B T}{h\, c}\, exp\left(-\frac{\Delta G}{k_B T}\right) \qquad (2-12)$$

where h, k_B and T are Plank's constant, Boltzmann constant and absolute temperature respectively. c is the standard-state concentration and is often considered 1 mol/dm^3 [63]. G is the Gibbs energy and defined by this formula:

$$G = U + PV - TS \qquad (2-13)$$

The change in Gibbs energy is calculated by:

$$\Delta G = \Delta U + \Delta(PV) - \Delta(TS) \qquad (2-14)$$

With the assumption of constant pressure, volume and temperature, ΔG can be estimated by the following formula:

$$\Delta G = \Delta U - T\Delta S \qquad (2-15)$$

ΔU is the difference between internal energy of the stacked and fully exfoliated structures which is also called energy barrier of exfoliation. ΔS is the difference between enthalpies of the stacked and exfoliated structures. S is calculated using this formula [64]:

$$S = k_B \ln q + k_B T \left(\frac{\partial (ln\, q)}{\partial T}\right)_{N,V} \qquad (2-16)$$

where q is the partition function and ΔS is easily calculated using the relation:

$$\Delta S = S_2 - S_1 = k_B\, ln\left(\frac{q_2}{q_1}\right) + k_B T \left(\frac{\partial \left(ln\left(\frac{q_2}{q_1}\right)\right)}{\partial T}\right)_{N,V} \qquad (2-17)$$

where q_1 and q_2 are partition functions for stacked and exfoliated structures respectively. For determining these partition functions, different micro-scale energy storage modes in the structures are considered. The main micro-scale energy modes considered are translational, rotational and vibrational. Electronic and nuclear contributions are negligible [58]. After substituting all partition functions in the relation, it is concluded that [65]:

$$\Delta S = k_B \left\{ ln\left(\frac{\left(\theta_{rot1,x}\, \theta_{rot1,y}\, \theta_{rot1,z}\, \pi\, T^3\right)^{\frac{1}{2}}}{\theta_{rot2,x}\, \theta_{rot2,y}\, \theta_{rot2,z}}\right) + \sum_{i=1}^{6} ln\left(\frac{1 - exp\,(-h\nu_i/k_B T)}{exp\,(-h\nu_i/2k_B T)}\right)\right\}$$

$$+ k_B T \left[\sum_{i=1}^{6} \left\{\left(\frac{h\nu_i}{2k_B T^2}\right)\left(\frac{exp\,(-h\nu_i/k_B T) + 1}{exp\,(-h\nu_i/k_B T) - 1}\right)\right\} + \frac{3}{2}\left(\frac{1}{T}\right)\right] \qquad (2-18)$$

$\theta_{rot1,x}$, $\theta_{rot1,y}$ and $\theta_{rot1,z}$ are characteristic temperatures of rotation for the stacked structure around the x, y and z axes respectively and calculated according to the following relation. Only $\theta_{rot1,x}$ is explained here and the other two terms are calculated in a similar way:

$$\theta_{rot1,x} = \frac{h^2}{8\,\pi^2\, I_{1,x}\, k_B} \qquad (2-19)$$

$I_{1,x}$ is moment of inertia of the whole molecule (including both stacked sheets) around the x axis. It is assumed that the molecule's mass center is located on the origin of the Cartesian coordinate system while each x and y axes are parallel to one side of the square sheets and the z axis is perpendicular to both sheets. Relation 2-18 is valid only when $T \gg \theta_{rot1,x}, \theta_{rot1,y}, \theta_{rot1,z}$ which is true for our calculations as it will be shown in the results chapter.

There are six different ν_i in the relation 2-18 based on different values for i from 1 to 6. It is worth mentioning that for determining the vibrational partition function of the stacked structure, six different motions of the two sheets relative to each other that generate six different vibrational modes are considered (Fig. 11).

Half of the six intersheet vibrational modes are created due to linear infinitesimal motions of the two sheets along and parallel to the x, y and z directions but in the opposite directions. For example when one sheet moves in the positive x direction, the other one moves in negative x direction and vice versa while during the entire motion both sheets remain parallel to x axis. At these three modes, the sheets do not rotate around any of the three Cartesian axes. The other three vibrational modes are generated when two sheets tilt infinitesimally around x, y and z axes but in opposite directions. So i in relation 2-18 represents six different vibrational modes and ν_i is vibrational frequency.

The frequency of vibration, or ν_i, for the three vibrational modes generated by the translational motions of the two sheets are calculated by this formula:

$$\nu = \frac{1}{2\pi}\left(\frac{k}{m_r}\right)^{\frac{1}{2}} \qquad (2-20)$$

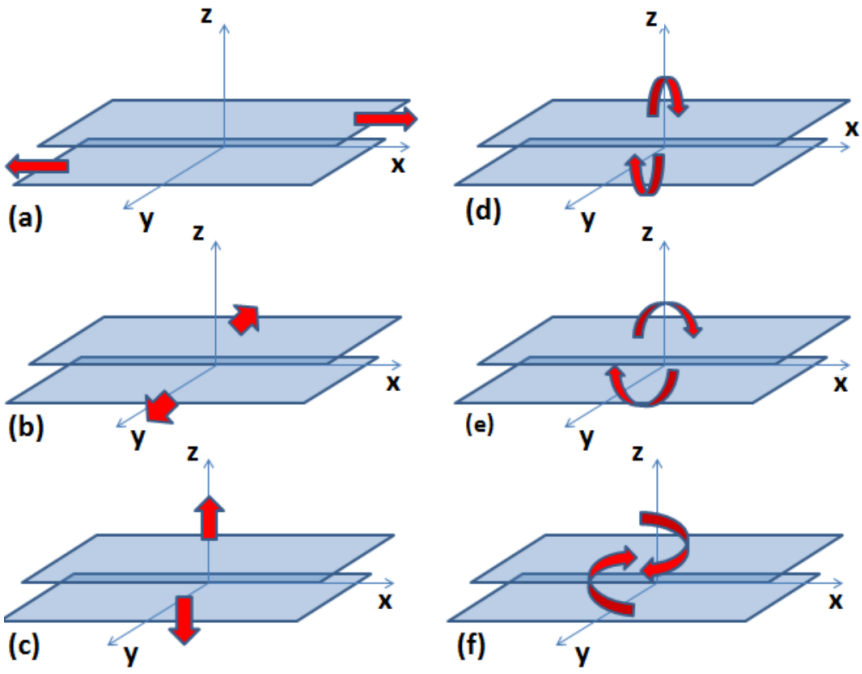

Figure 11: Representation of six relative infinitesimal motions of the two sheets with respect to each other [65].

where k is the effective force constant and m_r is the reduced mass using the masses of two single sheets of the structure. ν_i for three vibrational modes generated by rotational motions of the sheets is given by this formula:

$$\nu = \frac{1}{2\pi}\left(\frac{k}{I_r}\right)^{\frac{1}{2}} \qquad (2-21)$$

where I_r is the reduced moment of inertia using the moments of inertia of two single sheets of the structure relative to the axis around which they are rotating.

$\theta_{rot2,x}$, $\theta_{rot2,y}$ and $\theta_{rot2,z}$ are characteristic temperatures of rotation for the exfoliated structure around the x, y and z axes respectively. For calculating characteristic temperatures, it should be mentioned that in the exfoliated sheets, the moment of inertia

is calculated using atoms of only one single sheet relative to axes that pass through the mass center of that single sheet and not the mass center of the whole two-sheet molecule and origin of the Cartesian coordinate for each sheet is located on the mass center of that single sheet.

2.7 Electronic Band Structure

The band structure takes into account the periodicity of a crystal lattice by using symmetry operations that form a space group. According to Bloch's theorem [66], the wave function or solution of Schrödinger equation can be written as:

$$\Psi(r) = \sum_k \Psi_k(r) \sum_k A_k \exp(ikr)\, u_k(r) \qquad (2-22)$$

where k is used to index different solutions and is called the wave vectors of the plane waves of the Bloch function. $\Psi_k(r)$ are different solutions of Schrödinger equation. A_k is constant and $u_k(r)$ is defined as follows:

$$u_k(r + nT) = u_k(r) \qquad (2-23)$$

where n is any integer and T is any period vector of the periodic potential energy of Schrödinger equation. If electron energies that are specified by solving Schrödinger equation are plotted versus the wave vector (k), the resultant graph is called the electronic band structure.

The electronic band structure can be used to describe some physical properties of a solid. The amount of band gap is the most useful information an electronic bandstructure

provides. By using the band gap, many electrical and optical properties of materials like electrical conductivity can be predicted. The probability of the presence of an electron in different energy levels within the band is not the same. It goes to zero at the band boundaries while its maximum usually happens in the middle of the band. Many of the energy states within the bands are empty because the number of filled states cannot be more than the number of protons in the atom of an uncharged material. The probability of any given state being filled at a temperature of T is given by Fermi-Dirac relation:

$$f(E) = \frac{1}{1+e^{\frac{E-\mu}{K_B T}}} \qquad (2-24)$$

where K_B is Boltzmann constant, μ is chemical potential or Fermi level and T is absolute temperature.

2.8 Phonon Dispersion

In a static model of atoms in a lattice, the average position of each atom is considered to be its fixed position but in a dynamic model atoms are vibrating around their average position due to their interaction with neighboring atoms. These elastic vibrations of atoms in a lattice are called phonons and the relation between frequency of a phonon (ω) or its energy ($\hbar\omega$) and wave vector (k) is called phonon dispersion.

There are two modes of vibration [67]. The first one is the optical mode where there is a relative motion between two adjacent different atoms and this only happens when there are more than one atom in the unit cell and the second mode is acoustic where two atoms

move together and hence there is no relative motion between the atoms. The acoustic mode is the only mode for unit cells that include only a single atom.

One of the applications of phonon dispersion relation is determining speed of sound in a solid. Sound speed is the same as the propagation velocity of an acoustic phonon which in turn equals the slope of the phonon frequency relative to the wave vector changes in the phonon dispersion plot or $\frac{\partial \omega_k}{\partial k}$.

2.9 Specific Approaches, Settings, and Programs Used in This Study

The SIESTA software [68,69] that uses the DFT method is used in this work. For calculating exchange-correlation energy, LDA approximations with Ceperley-Alder (CA) pseudopotentials were used. For structural relaxations, a maximum force tolerance of 0.03 eV/Å has been used for energy calculations, while for electronic band structures and phonon dispersion a maximum force tolerance of 0.0005 (eV/Å) was considered. Graphene's phonon dispersion was calculated using Perdew-Burke-Ernzerhof (PBE) version of GGA. The basis set was Double Zeta basis with polarization (DZP). Each unit cell used in the single-layer calculations included 8 carbon atoms along with bonded atoms while for bilayer structures, unit cells had 16 carbon atoms with corresponding bonding atoms. For water intercalation and lithium adsorption calculations, unit cell contained two carbon atoms plus corresponding extra atoms. k-grid cut off of 80 Bohr were used. Mesh cutoff of 250 Ry was used for the setting of SIESTA. All UFF calculations were performed using GAUSSIAN 09 suite of programs [70].

2.10 Validation of Method: Electronic Band Structure and Phonon Dispersion of Graphene

For validating our calculation of electronic band structure and phonon dispersion of 4 graphene oxide structures, these curves for pristine graphene were calculated. They are shown in Fig. 12. Electronic band structure of graphene is the same as what is pubilshed in [71] and phonon dispersion curve coincides exactly with what is pubilshed in [72].

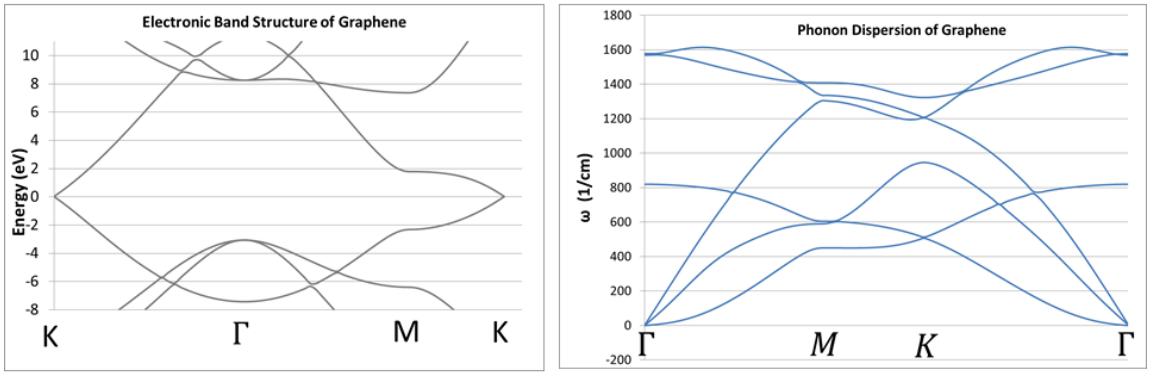

Figure 12: Electronic band structure and phonon dispersion of pristine graphene

3. RESULTS AND DISCUSSIONS

For calculating the exfoliation rate in graphene oxide, 12 different bilayer, 40 Å square structures have been chosen. These 12 structures include two different levels of oxygen coverage (50 and 100%), two different stacks (AA or AB), two different types of functional groups bonded to carbon atoms including epoxy (O) and hydroxyl (OH), and two different relative positions of these groups on the top and bottom layers (coincide and non-coincide). For making these structures, in the first step, a single layer periodic unit cell of four structures have been relaxed using SIESTA. Each unit cell includes 8 carbon atoms along with either of these two functional groups. Then 12 bilayer structures using one-layer relaxed structures have been made and relaxed. The results of the first run of relaxation are then used to calculate UFF energies versus interlayer distance for 40 Å square sheets. This in turn determines the stable interlayer distance, with strong van der Waals interactions, indicated by minimum UFF energy. A second step in SIESTA relaxation is then carried out to determine the LDA energies of the structures. The updated minimum (LDA) energy distance is then used in a series of subsequent UFF calculations for 40 Å sheets to determine the force constants. Entropy, exfoliation energy barriers, and exfoliation rates are then calculated. We also include the effects of water solvent. Intercalation of water molecules between the sheets and its effect on exfoliation is discussed. Results on electronic band structure of graphene oxide with various oxygen coverages are presented. We also calculate and discuss lithium storage characteristics of our structures with 100% oxygen coverage.

3.1 Single-Layer Graphene Oxide Structures Used in This Study and Their Characteristics

Four single layer unit cells relaxed in the first step are 50-GO, 100-GO, 50-GOH and 100-GOH. These structures are shown in Fig. 13. Regarding oxygen coverage of each structure, as it is seen in Fig. 13, 50% and 100% coverage levels are considered. 50% means half of the carbon atoms in graphene are bonded to oxygen atoms and 100% means all carbon atoms are bonded to oxygen atoms. There are two different functional groups bonded to carbon atoms of graphene. In GO structures, each oxygen atom is adsorbed on a bridge site meaning each oxygen atom is bonded to two carbon atoms. In GOH structures, each OH group is connected to one carbon atom. In both GO and GOH structures, the number of oxygen groups are the same at each side of the sheets.

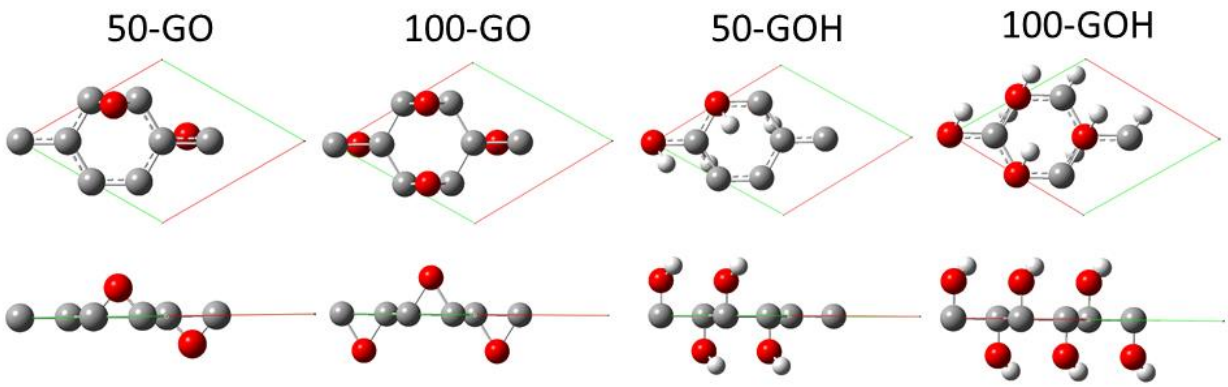

Figure 13: Four different 8 carbon-atom unit cells of single-layer periodic graphene structures with various oxidation patterns whose geometries were optimized: Graphene oxide with 50% of carbon atoms covered with oxygen bridges (50-GO), graphene oxide with 100% of carbon atoms covered with oxygen bridges (100-GO), graphene oxide with 50% of carbon atoms covered with OH groups (50-GOH) and graphene oxide with 100% of carbon atoms covered with OH groups (100-GOH). For each structure, top and side views are depicted.

Adsorption energy is an indicator of bonding energies of oxygen or OH groups adsorbed on graphene while cohesive energy is used to describe overall stability of the structure [73]. The following relations are used for calculating adsorption and cohesive energies of GO and GOH structures:

$$E_{Adsorption-GO} = \frac{1}{N_O}(E_{graphene} + N_O E_O - E_{GO}) \quad (3\text{-}1)$$

$$E_{Adsorption-GOH} = \frac{1}{N_{O-H}}(E_{graphene} + N_{O-H} E_{O-H} - E_{GOH}) \quad (3\text{-}2)$$

The following equations are used for cohesive energies of GO and GOH structures, respectively:

$$E_{Cohesive-GO} = \frac{E_{GO} - N_C E_C - N_O E_O}{N_C + N_O} \quad (3\text{-}3)$$

$$E_{Cohesive-GOH} = \frac{E_{GOH} - N_C E_C - N_O E_O - N_H E_H}{N_C + N_O + N_H} \quad (3\text{-}4)$$

Here N_H, N_C, N_O and N_{OH} are the number of hydrogen, carbon, oxygen atoms and OH groups in the structure respectively. E terms are total energy of each structure or atom. Table 1 shows the calculated adsorption and cohesive energies for different periodic unit cells of graphene oxide.

Table 1**:** Adsorption and cohesive energy of different single-layer periodic structures.

Structure	Adsorption Energy (eV/ adsorbed molecule)	Cohesive Energy (eV/ atom)
50-GO	4.687	-8.598

100-GO	5.198	-8.116
50-GOH	4.174	-7.261
100-GOH	4.380	-6.558

According to the values calculated for adsorption energies, chemical bonds between oxygen atoms and graphene are stronger in the 100-GO structure than those in the 50-GO structures. Chemical bonds between OH groups and graphene are also stronger in the 100-GOH structure than those in the 50-GOH structure. Therefore, the adsorbing atoms show clustering behavior, the same as what was observed for hydrogenation of silicene [74]. It means they have stronger attachment to the sheet if they attach in more dense coverage. Table 1 also shows that O bridges are more strongly bonded to graphene lattice than OH groups. This is attributed to double bond connection for O bridges versus single bond connections for OH groups.

Comparing cohesive energies of these 4 structures shows GO structures have lower energies. This means GO structures are more stable than GOH structures. This is again attributed to double-bond (i.e. more stable) connection of O bridges.

3.2 Electronic Band Structure of Graphene Oxide

Electronic band structure of single-layer 50-GO, 100-GO, 50-GOH and 100-GOH structures are depicted in Fig. 14. As it can be seen from the Fig. 14, for low oxygen coverage structures of 50-GO and 50-GOH, band gap is zero like pristine graphene and they are conductors; but by increasing oxygen coverage the band gap opens and the

structures become insulators. It means that using graphene oxide with high oxygen coverage for devices where high conductivity is needed, such as cathode material of Li-ion batteries, a conductive additive like carbon black is needed. The pattern of changing bandgap with oxygen coverge is consistent with a study done by Huang, et al. [56] despite the fact that they considered oxygen only on one side of the carbon lattice while in our study, oxygen atoms are considered on both sides of it. The 100-GO structure that has 50% oxygen coverage has about a 3 eV bandgap. It is equal to the bandgap in 50% coverage in Ref. [56]. However, 50-GO structure with 25% oxygen coverge in our study has zero bandgap while in Fig. 9 it has about 0.4 eV.

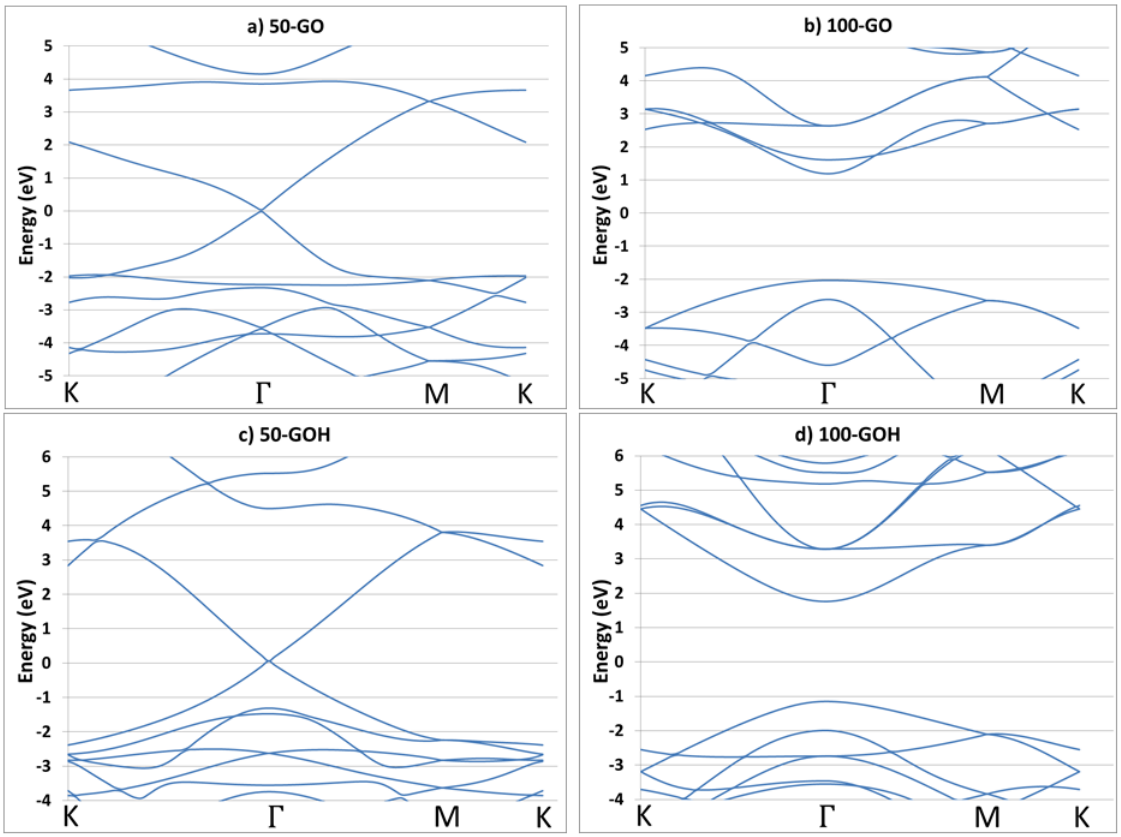

Figure 14: Electronic band structure of single-layer 50-GO, 100-GO, 50-GOH and 100-GOH structures. Fermi energy is shifted to zero.

3.3 Bilayer Graphene Oxide Structures Used in This Study and Their Characteristics

After all 4 structures in the first step were relaxed, 12 bilayer structures using one-layer relaxed structures have been made. All of these 12 structures are shown in Figs. 15, 16 and 17. Initial interlayer distances for all these structures is around 3.3-4.3 Å. This distance is measured between the highest atom at the bottom layer and the lowest atom at the top layer. The exact value of initial interlayer distance does not affect our final structures as the outputs of the first SIESTA relaxation will go through other UFF and SIESTA relaxation stages.

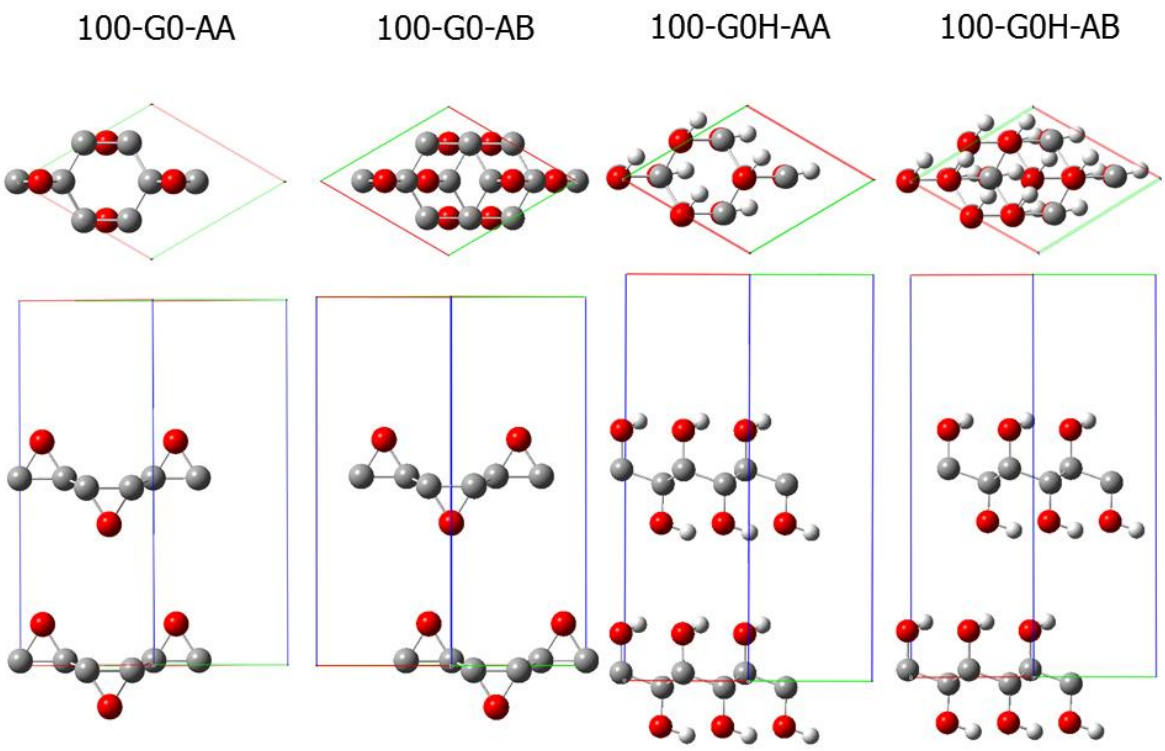

Figure 15: Four bilayer structures with 100% oxygen coverage. Upper panels show top views and bottom ones show side views of the structures. Two different bilayer structures are made using AA and AB stacks for each 100-GO and 100-GOH.

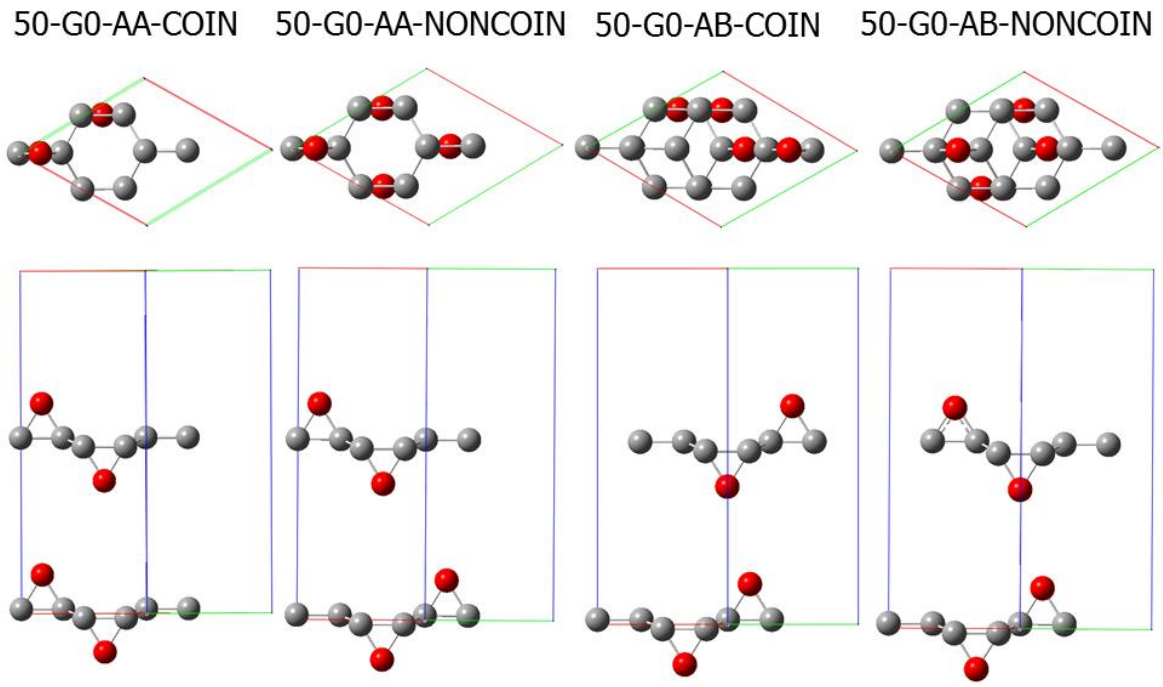

Figure 16: Four bilayer structures with 50% oxygen coverage of GO. Upper panels show top views and bottom ones show side view of the structures. Two different bilayer structures are made using AA and AB stacks for each 50-GO structure. Besides those AA and AB, there are two more coincide and non-coincide structures. For coincide structures, positions of adsorbed groups are the same at the top and bottom layers but for non-coincide structures, their locations are different at the two layers.

For 100% coverage of both GO and GOH structures, as it can be seen in Fig. 15, two different bilayer structures can be made using two different AA and AB stacks. The same holds true for 50% structures as they can be seen in Figs. 16 and 17. Besides those AA and AB stacks, there are two more structures for 50% structures: coincide and non-coincide structures. For coincide structures, positions of functional groups are the same at top and bottom layers but for non-coincide structures, their locations are different at the two layers as it can be seen in Figs. 16 and 17.

These 12 bilayer structures have been relaxed again using the LDA method. For bilayer structures with weak van der Waals forces between 2 layers, LDA is a better method than

GGA [75]. Full relaxation has been done until the maximum force on each atom is less than 0.01 (eV/Å). During relaxation, interlayer distances approximately remained the same. It means for the chosen initial interlayer distances, van der Waals interactions between the two layers are small. For 50-GOH-AA-NONCOIN, however, the first SIESTA relaxation resulted in significant reduction in interlayer distance. As we shall see shortly this is in fact consistent with the result of the second SIESTA relaxations for all structures.

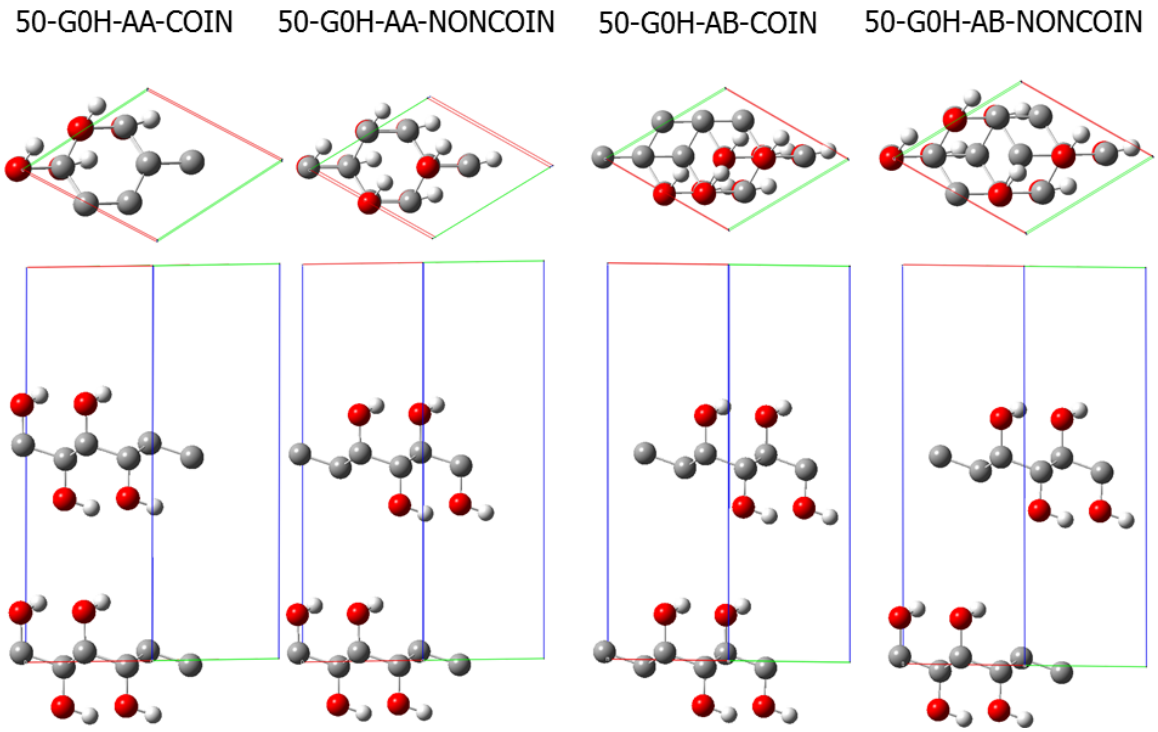

Figure 17: Four bilayer structures with 50% oxygen coverage of GOH. Upper panels show top views and bottom ones show side view of the structures. Two different bilayer structures can be made using AA and AB stacks for each 50-GOH structure. Besides those AA and AB, there are two more coincide and non-coincide structures. For coincide structures, positions of adsorbed groups are the same at top and bottom layers but for non-coincide structures, their locations are different at the two layers.

Since the purpose of making those structures is for exfoliation calculation, their periodic structures cannot be used directly and square structures of them were needed. Therefore, in the next step, the 12 periodic bilayer relaxed structures were extended to 40 Å bilayer square sheets. Although in a previous study [65], 80 Å platelet size was shown to result in converged energy barrier values for pristine graphene, 40 Å is considered here owing to increased complexity and computational effort of graphene oxide structures as compared to pristine graphene. Then UFF calculations were used for all 40 Å square bilayer structures in the next step. UFF calculations were carried out to obtain the interlayer distance that minimizes total energy of each structure. It means every structure whose total energy is evaluated by UFF method has the same x and y coordinates as in LDA relaxed structure but is shifted along the z axis to get different interlayer distances. The UFF method was used because it provides relatively satisfactory results for big structures in a short calculation time. The energies of each structure versus the interlayer distance are shown in Figs. 18, 19 and 20.

It can be seen from Figs. 18, 19 and 20 that for most of the structures, the interlayer distance that minimizes the total energy is less than the interlayer distance of the relaxed structures by LDA. The only exception is the 50-GOH-AA-NONCOIN structure where an interlayer distance of minimum energy is more than the interlayer distance of the relaxed structures by LDA.

Since the results of UFF show different interlayer distances which were not predicted by the first step of the LDA relaxation, the second LDA relaxations were carried out for all 12 structures using estimated interlayer distances of the structures with the minimum energy by UFF calculations to reveal the relative configuration of the 2 layers.

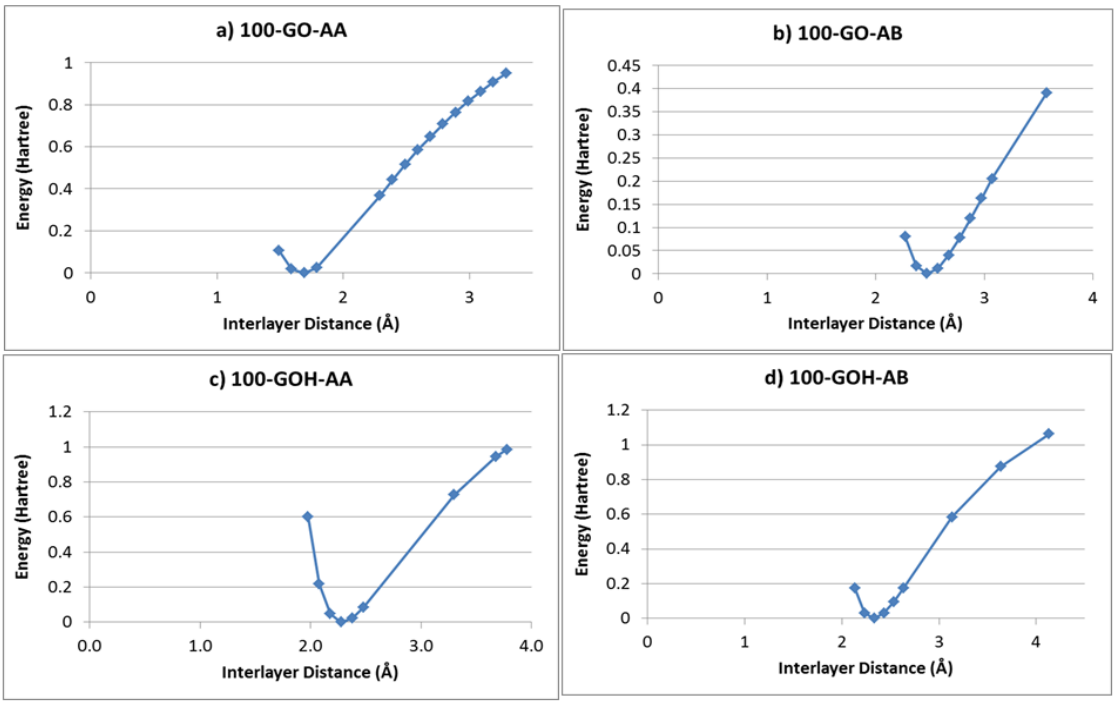

Figure 18: Total energy calculation by UFF for 100-GO-AA, 100-GO-AB, 100-GOH-AA and 100-GOH-AB structures. Zero energy corresponds to minimum energy value.

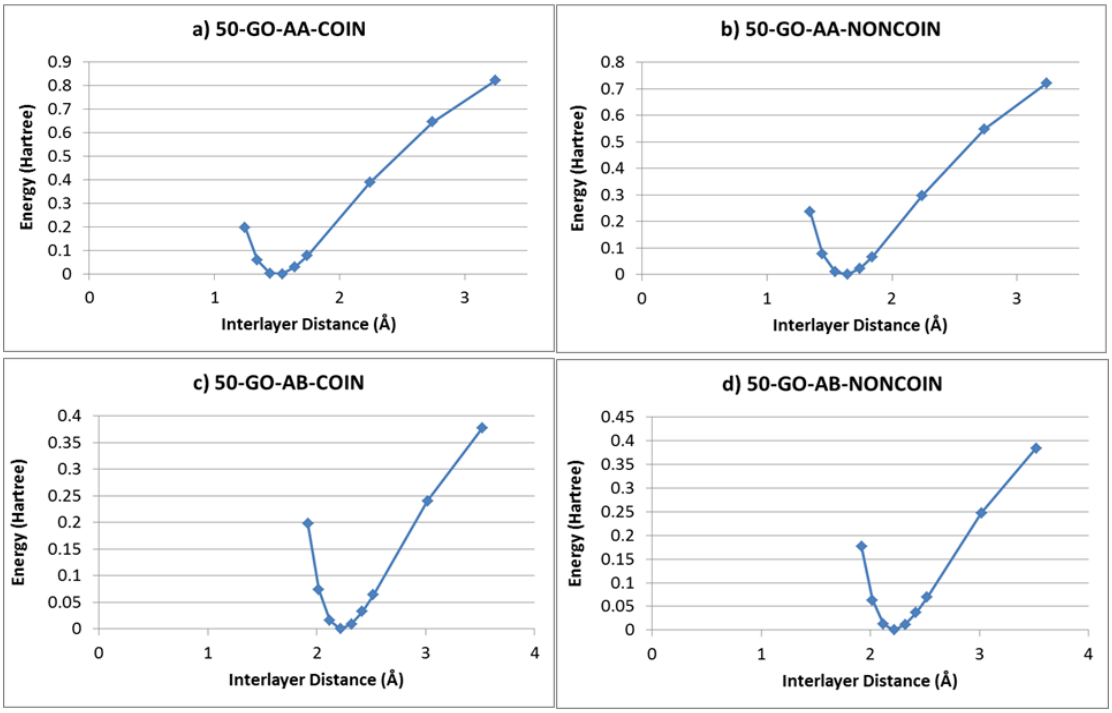

Figure 19: Total energy calculation by UFF for 50-GO-AA-COIN, 50-GO-AA-NONCOIN, 50-GO-AB-COIN and 50-GO-AB-NONCOIN structures. Zero energy corresponds to minimum energy value.

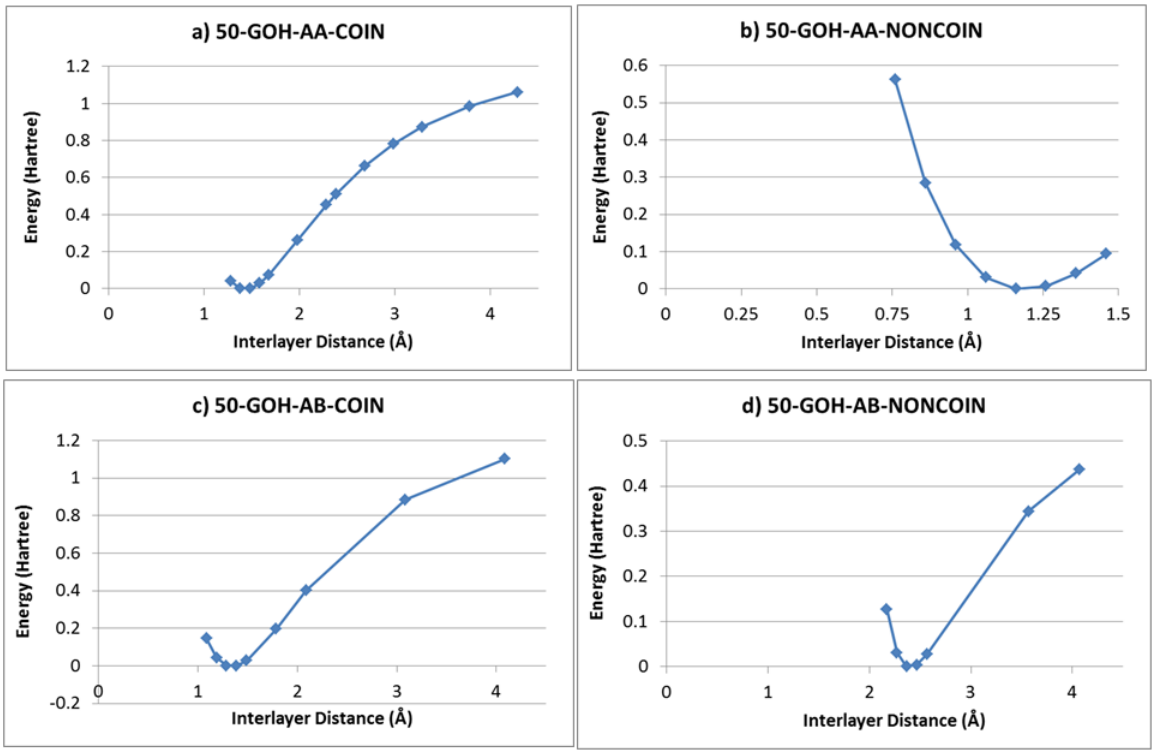

Figure 20: Total energy calculation by UFF for 50-GOH-AA-COIN, 50-GOH-AA-NONCOIN, 50-GOH-AB-COIN and 50-GOH-AB-NONCOIN structures. Zero energy corresponds to minimum energy value. For 50-GOH-AA-NONCOIN, the minimum energy distance turned out to be almost that of second step SIESTA relaxation.

The structures relaxed by the second SIESTA step are shown in Figs. 21, 22 and 23. As it can be seen from Fig. 21, 100-GO-AA and 100-GO-AB structures have exactly the same atomic coordinates and interlayer distance after the second relaxation. The same holds true for 50-GO-AB-COIN and 50-GO-AB-NONCOIN structures. This may not be seen directly in Fig. 22, owing to the tilted nature of the unit cell, but if unit cells of these 2 structures are repeated, they turn out to have the same lattice. 50-GOH-AA-COIN, 50-GOH-AA-NONCOIN and 50-GOH-AB-COIN structures in Fig. 23, also have the same atomic coordinates and interlayer distances.

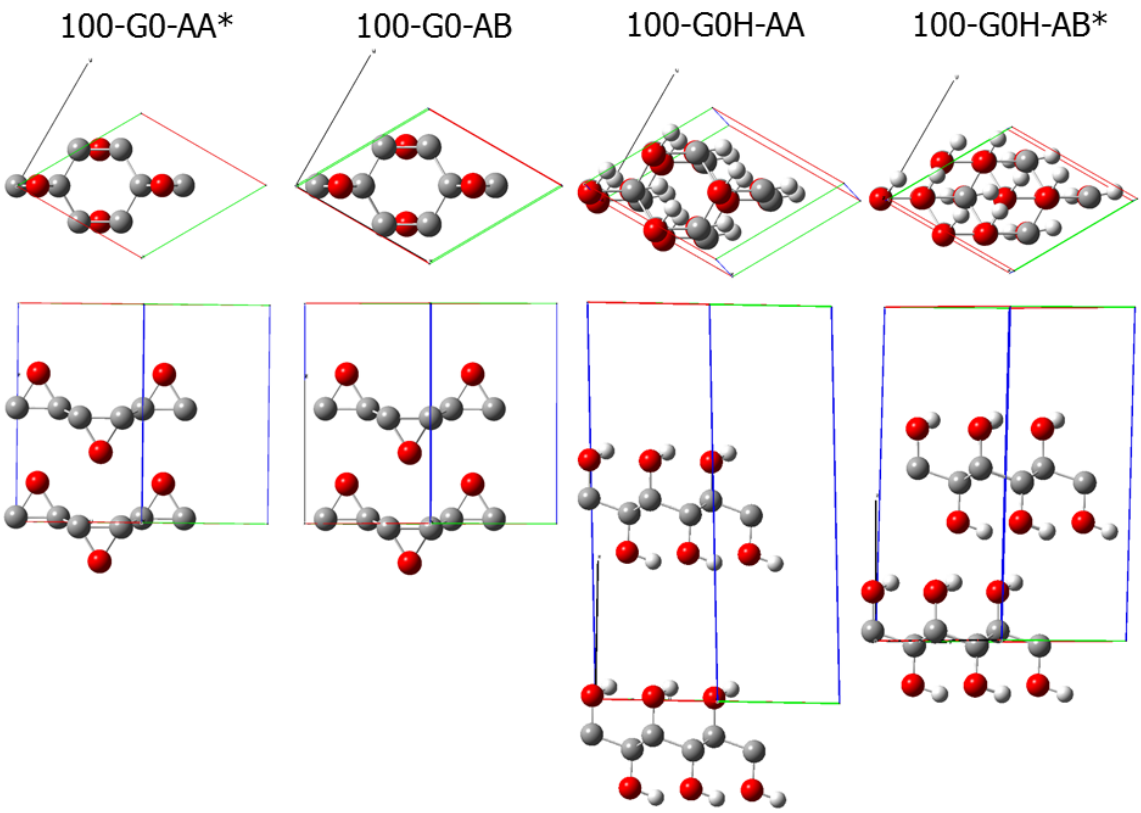

Figure 21: Four structures with 100% oxygen coverage after the second run of SIESTA. Top panels show top views and bottom ones show side views of the structures. 100-GO-AA and 100-GO-AB structures have exactly the same atomic coordinates and interlayer distance. The structures indicated by * are the ones with minimum energy that were chosen to represent a group of relaxed structures.

Table 2 shows interlayer distance and cohesive energy of all structures after second run of SIESTA. 100-GO-AA and 100-GO-AB structures become the same after relaxation; therefore one of them (100-GO-AA) was chosen for exfoliation rate calculations. From Table 2 it is observed that among four 50-GO structures, 50-GO-AA-NONCOIN structure has at least 31 meV higher cohesive energy than the other 3 structures and therefore it was less stable. This structure was not considered for the rest of calculations. 50-GO-AB-COIN and 50-GO-AB-NONCOIN structures have exactly the same atomic coordinates and interlayer distances and both have 2 meV lower cohesive energy than 50-

GO-AA-COIN structure. Therefore one of them (50-GO-AB-COIN) was used for exfoliation rate calculations. Regarding four 50-GOH structures, 50-GOH-AA-COIN, 50-GOH-AA-NONCOIN and 50-GOH-AB-COIN are the same. These 3 structures have lower cohesive energy than 50-GOH-AB-NONCOIN structure. Thus, one of those 3 similar structures (50-GOH-AA-NONCOIN) was used. As for two 100-GOH structurs, 100-GOH-AB was used due to its lower cohesive energy compared to 100-GOH-AA structure.

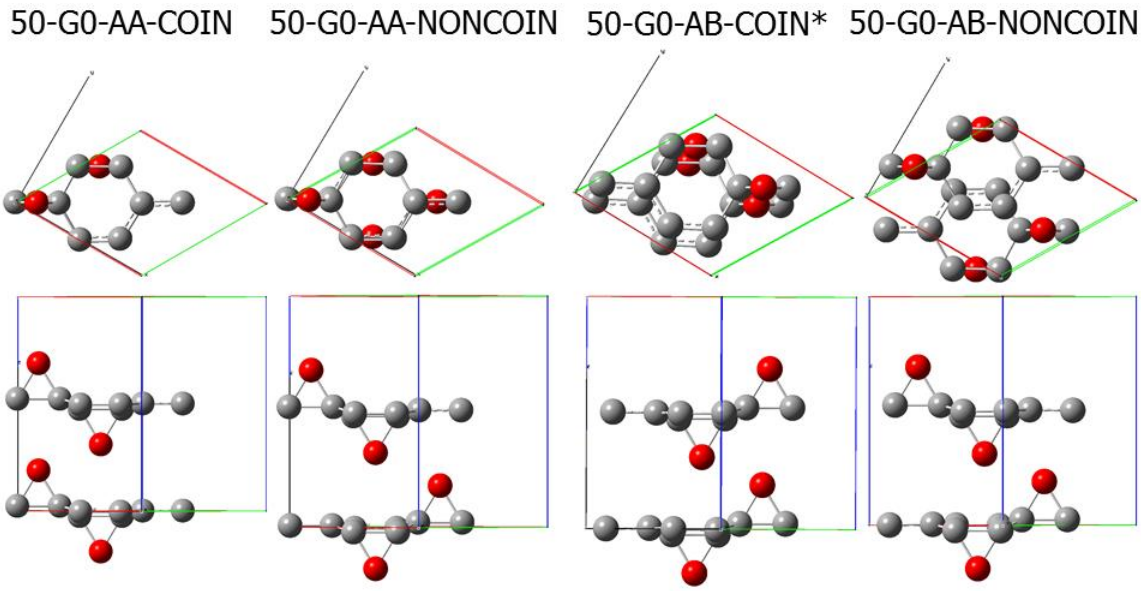

Figure 22: Four structures with 50% oxygen coverage of GO after the second run of SIESTA. Top panels show top views and bottom ones show side views of the structures. Repeating 50-GO-AB-COIN and 50-GO-AB-NONCOIN unit cells shows they have the same atomic coordinates and interlayer distance. The structure indicated by * is the one with minimum energy that were chosen to represent a group of relaxed structures.

From Table 2 we observed that, the difference in cohesive energies indicate more stability of 50% structures compared to their corresponding 100% structures, and more stability of GO structures with respect to the GOH structures with the same coverage ratio. A more detailed investigation indicate that for the GO cases the distances between

the two carbon lattices are ~ 3.8 Å while for the GOH cases the distances between the two carbon lattices are ~ 4.5 Å. As the former value is closer to the interlayer distance in pristine graphite and considering the fact that for lower surface coverages the dominant interactions is between the carbon lattices, one can expect more stability for the GO structures especially at low coverage.

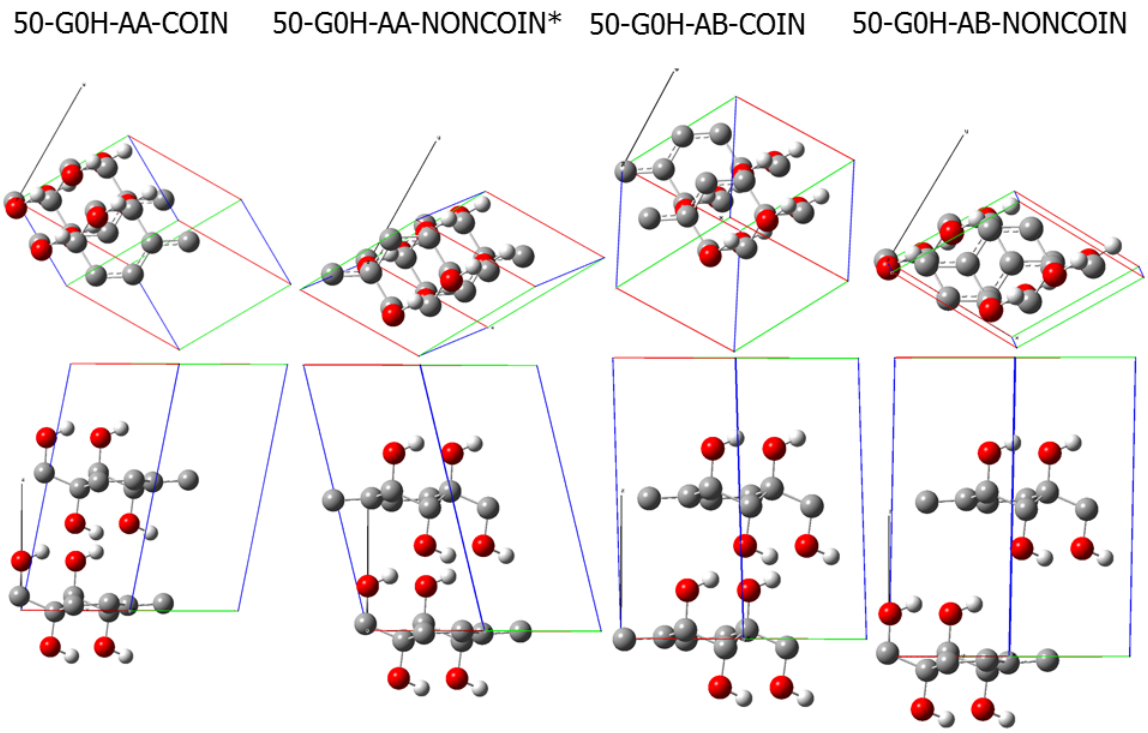

Figure 23: Four structures with 50% oxygen coverage of GOH after the second run of SIESTA. Top panels show top views and bottom ones show side views of the structures. The structure indicated by * is the one with minimum energy that were chosen to represent a group of relaxed structures.

In Table 3 van der Waals interaction energy for all 4 selected bilayer structures can be seen. These energies have been calculated using the following formula:

$$E_{vdW} = E_{t,2} - 2E_{t,1} \qquad (3-5)$$

Table 2: Interlayer distance and cohesive energy of all 12 structures after the second run of SIESTA for LDA relaxation. The structures indicated by * represent the most stable structure considered for reaction rate calculations.

STRUCTURE	Cohesive Energy (eV/atom)	Interlayer Distance (Å)
100-G0-AA*	-8.284	1.10
100-GO-AB	-8.284	1.10
50-GO-AA-COIN	-8.725	0.90
50-GO-AA-NONCOIN	-8.694	1.09
50-GO-AB-COIN*	-8.727	0.88
50-GO-AB-NONCOIN	-8.727	0.88
50-GOH-AA-COIN	-7.331	0.75
50-GOH-AA-NONCOIN*	-7.331	0.75
50-GOH-AB-COIN	-7.331	0.73
50-GOH-AB-NONCOIN	-7.317	1.45
100-GOH-AA	-6.573	4.57
100-GOH-AB*	-6.583	1.81

Where,

E_{vdW} : van der Waals interaction energy per unit cell

$E_{t,2}$: total energy of bilayer structure per unit cell

$E_{t,2}$: total energy of single-layer structure per unit cell

Table 3: Van der Waals interaction energy for all 4 bilayer structures

Structure	Energy $(eV/unit\ cell)$
50-GO-AB-COIN	-2.487
50-GOH-AA-NONCOIN	-2.042
100-GO-AA	-3.772
100-GOH-AB	-0.736

Comparing values in Table 3 shows that in GO structures the interactions between the two sheets due to van der Waals forces are stronger than the interactions between them in GOH structures. This is again attributed to the smaller interlayer distances for the GO structure as compared to GOH ones.

3.4 Force Constant Calculations

As it was mentioned in section 2-6, for calculating vibrational partition function in stacked structures, six different motions of the two sheets relative to each other that generate six different vibrational modes are considered. Three of these six inter-sheet

vibrational modes are created due to very small relative linear motions of the two sheets along and parallel to x, y and z directions but in the opposite directions. The other three vibrational modes are generated when two sheets rotate in very small angles around x, y and z axes in opposite directions. For calculating vibrational frequency according to equations 2-20 and 2-21, force constants of vibrational motions need to be calculated first. They are calculated using UFF total energy calculations around the minimum energy structures obtained from second SIESTA relaxations. UFF energy calculations provide us with energy values that are then fitted with second-order polynomials with respect to the corresponding distance/angle change. The coefficients of the second order terms are one-half of the corresponding force constants. Calculated force constants are presented in Table 4.

Table 4: Calculated force constants of six different vibrational modes due to different translational or rotational motions of the two sheets relative to each other.

Force Constants						
Structure	**Translational K** $(kg\ s^{-2})$			**Rotational K** $(10^{-15} kg\ m^2 s^{-2})$		
	K_x	K_y	K_z	K_x	K_y	K_z
50-GO-AB-COIN	402.9	108.1	1665.0	217	216	0.807
50-GOH-AA-NONCOIN	635.5	1829.9	1393.7	169	163	3.01
100-GO-AA	874.9	206.4	1942.4	264	256	1.47
100-GOH-AB	162.3	74.6	4020.9	509	537	.0486

Values in Table 4 show that force constants of all 4 graphene oxide structures related to translational modes in x and y directions are larger than their corresponding values for pristine graphene [65], but in z direction they are of the same order. Force constants of rotational induced modes are a few orders of magnitude bigger than those of pristine graphene. The adsorbed groups on carbon lattice (O bridge or OH) prevent smooth sliding/tilting as it occurs in pristine graphene. The reason is explained using equation 2-11. In graphene oxide structures, distance between two layers (vertical distance between nearest atoms from the 2 layers) is lower than that of pristine graphene. Therefore, the terms like R^{-12} in total energy are much more sensitive to change of distance.

3.5 Exfoliation Rate Calculations

Before calculating exfoliation rate according to relation 2-12, there are a few parameters that need to be known first. Calculated moments of inertia for different structures can be seen in Table 5. $I_{1,x}$, $I_{1,y}$ and $I_{1,z}$ are moments of inertia of the whole bilayer stacked structures around x, y and z axes respectively. $I_{2,x}$, $I_{2,y}$ and $I_{2,z}$ are moment of inertia for a single sheet in exfoliated structures. Table 6 shows reduced masses and moments of inertia for all 4 structures.

In Table 7 characteristic temperatures of rotation for stacked ($\theta_{rot1,x}$, $\theta_{rot1,y}$, $\theta_{rot1,z}$) and exfoliated ($\theta_{rot2,x}$, $\theta_{rot2,y}$ and $\theta_{rot2,z}$) structures around x, y and z axes are shown. These parameters are used for calculation of entropies. As it was mentioned in section 2-6, Relation 2-18 is valid only when $T \gg \theta_{rot1,x}, \theta_{rot1,y}, \theta_{rot1,z}$ which is true for our calculations at room temperature (T=298 K) as it can be seen from the Table 7.

Table 8 shows calculated vibration frequencies for all 6 vibration modes for each structure. As it was mentioned earlier, these vibration modes are due to six different motions of the two sheets relative to each other. Three of them are created due to relative linear infinitesimal motions of the two sheets with respect to each other and the others are generated when two sheets tilt infinitesimally relative to each other around each of the three catresian axes. Subscripts x, y and z are used to show direction of motion for translational and rotational modes respectively.

Table 9 shows entropy changes between stacked and fully exfoliated structures. These values are calculated using relation 2-18.

Table 5: calculated moments of inertia for different structures: $I_{1,x}$, $I_{1,y}$ and $I_{1,z}$ are moments of inertia of the whole bilayer stacked structures while $I_{2,x}$, $I_{2,y}$ and $I_{2,z}$ are moment of inertia for a single sheet in exfoliated structures around 3 axes of Cartesian coordinates.

Moment of Inertia $(10^{-41}\ kg\ m^2)$						
Structure	$I_{1,x}$	$I_{1,y}$	$I_{1,z}$	$I_{2,x}$	$I_{2,y}$	$I_{2,z}$
50-GO-AB-COIN	5.16	5.50	10.30	2.50	2.67	5.15
50-GOH-AA-NONCOIN	6.38	6.33	11.99	3.03	3.00	5.98
100-GO-AA	6.70	6.99	13.20	3.25	3.39	6.60
100-GOH-AB	9.74	9.93	18.28	4.55	4.67	9.12

Table 6: Reduced mass and moment of inertia for all 4 structures

Reduced Mass ($10^{-24}\ kg$) and Reduced Moment of Inertia ($10^{-41}\ kg\ m^2$)				
Structure	m_r	$I_{r,x}$	$I_{r,y}$	$I_{r,z}$
50-GO-AB-COIN	8.73	1.29	1.38	2.58
50-GOH-AA-NONCOIN	10.74	1.60	1.58	3.00
100-GO-AA	10.81	1.68	1.75	3.30
100-GOH-AB	15.16	2.44	2.48	4.57

7: Characteristic temperatures of rotation for stacked ($\theta_{rot1,x}$, $\theta_{rot1,y}$, $\theta_{rot1,z}$) and exfoliated ($\theta_{rot2,x}$, $\theta_{rot2,y}$ and $\theta_{rot2,z}$) structures around x, y and z axes.

Characteristic Temperature ($10^{-6}\ K$)						
Structure	$\theta_{rot,x,1}$	$\theta_{rot,y,1}$	$\theta_{rot,z,1}$	$\theta_{rot,x,2}$	$\theta_{rot,y,2}$	$\theta_{rot,z,2}$
50-GO-AB-COIN	7.80	7.32	3.91	16.12	15.09	7.82
50-GOH-AA-NONCOIN	6.31	6.36	3.36	13.30	13.42	6.74
100-GO-AA	6.01	5.76	3.05	12.41	11.89	6.10
100-GOH-AB	4.13	4.05	2.2	8.84	8.63	4.42

Table 8: Vibration frequencies for all 6 vibration modes of the structures

Vibration Frequency ($10^{11}\ s^{-1}$)						
Structure	**Translational Induced**			**Rotational Induced**		
	ν_x	ν_y	ν_z	ν_x	ν_y	ν_z
50-GO-AB-COIN	10.81	5.60	21.99	20.62	19.90	8.90
50-GOH-AA-NONCOIN	12.24	20.78	18.13	16.36	16.15	15.94
100-GO-AA	14.32	6.95	21.33	19.94	19.26	10.62
100-GOH-AB	5.21	3.53	25.92	22.98	23.41	1.64

Table 9: Calculated entropy changes between stacked and exfoliated structures

Structure	$\Delta S\ (eV/K)$
50-GO-AB-COIN	0.000957
50-GOH-AA-NONCOIN	0.001093
100-GO-AA	0.001038
100-GOH-AB	0.000817

Table 10 shows calculated energy barriers, changes in Gibb's energy and exfoliation rate. Energy barriers are calculated using difference in internal energy of stacked and exfolited 40 Å structures using UFF method at the same perpendicular interlayer distance. For calculating changes in Gibb's energy, relation 2-15 has been used. Gibb's energies are used to calculate exfoliation rate according to relation 2-12. Exfoliation rates are calculated for c = 1. For any other concentration, the exfoliation rates should be multiplied by the concentration and it will result in the number of exfoliation events per second for the corresponding amount of stacked graphene oxide per corresponding volume.

Table 10: Calculated differences in energy barriers, Gibbs energy and exfoliation rate for T=298K

Structure	$\Delta U\ (eV)$	$T\ \Delta S\ (eV)$	$\Delta G\ (eV)$	**Exf. Rate (1/s)**
50-GO-AB-COIN	34.607	0.285	34.332	6.42E-568
50-GOH-AA-NONCOIN	37.757	0.326	37.431	5.52E-621
100-GO-AA	41.089	0.310	40.779	2.06E-690
100-GOH-AB	38.676	0.243	38.433	1.01E-638

The calculated exfoliation rates turn out to be nearly zero. It should be mentioned that these rates are calculated when the plates are in vacuum.

3.6 Graphene Oxide Exfoliation in Solvent

In reality, exfoliation is performed under the effect of a solvent such as water. It is worth mentioning that this is different than the effect of intercalation of water molecules between the two sheets in the stacked state that will be discussed in next section. Water has relative dielectric constant of about 78.3, that is owing to water molecules polarizability in electric field. By putting the sample in water energy barrire ΔU will be divided by 78.3 compared to the case when the sample is in vacuum. Part of this reduction in energy is consumed for making new surface in water (otherwise would be a homogeneous liquid). So the generated surface energy of water should be added to energy barrier. Surface energy of water is $71.9 \times 10^{-3} \frac{J}{m^2}$. By applying the effects of both permittivity (dielectric constant) of water that reduces energy barrier and added surface energy of water that increases energy barrier, and ignoring small changes in entropy ΔS, new energy barriers, change in Gibbs energy and exfoliation rates were calculated and the results are shown in Table 11. Comparing energy barriers in Table 11 shows that energy barriers are almost the same after inclusion of water permittivity and surface energy.

As the values in Table 11 show, using water as solvent causes exfoliation to happen much faster. This means the effect of permittivity of water in reducing enegy barrier surpasses the effect of generating new water surface in increasing it.

3.7 Effect of Water Intercalation Between The layers

Unlike pristine graphene that is hydrophobic, graphene oxide, due to oxygen atoms on the surface, is hydrophilic. This is due to hydrogen bonds between hydrogen in water molecules and oxygen in graphene oxide or hydrogen bonds between oxygen of water molecule and hydrogen in GOH structures as it can be seen in Fig. 24. The amount of water molecules between two layers of graphene oxide depends on the humidity of the surrounding.

Table 11: Calculated differences in energy barriers, Gibbs energy and exfoliation rate upon including water permittivity and surface energy for *T=298*K

Calculated Energy Barriers, Gibbs Energy and Exfoliation Rate with using water as solvent				
Structure	$\Delta U\ (eV)$	$T\ \Delta S\ (eV)$	$\Delta G\ (eV)$	**Exf. Rate (1/s)**
50-GO-AB-COIN	14.798	0.315	14.483	6.9078E-233
50-GOH-AA-NONCOIN	14.838	0.326	14.512	2.2525E-233
100-GO-AA	14.881	0.310	14.571	2.2665E-234
100-GOH-AB	14.850	0.303	14.547	5.7344E-234

Presence of water molecules between the graphene oxide layers increases interlayer distance beyond the equilibrium arrangement. This causes energy to increase, as can be seen from Figs. 18, 19 and 20. As examples of including the effect of increased interlayer distance, energy barriers for output structures of the first run of SIESTA that have higher

interlayer distances have been calculated. This energy for 50-GOH-AA-NONCOIN is not calculated because interlayer distance for this structure in the first and second run of SIESTA are the same. Calculated energy barriers for large interlayer distances are shown in Table 12, without including the effects of water permittivity and surface energy. Comparing energy barriers in Tables 10 and 12 shows considerable reduction in energy barrier which in turn increases exfoliation rate significantly.

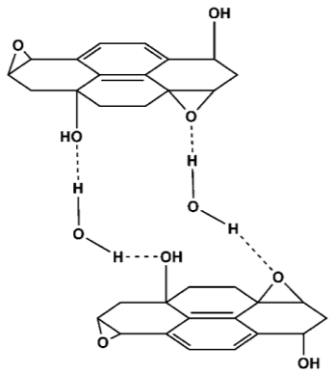

Figure 24: Hydrogen boding between intercalated water molecules and graphene oxide layers [6].

Table 12: Calculated energy barrier of the structures after the first run of SIESTA with higher interlayer distance.

Structure	$\Delta U\ (eV)$
50-GO-AB-COIN	8.552
50-GOH-AA-NONCOIN	-

100-GO-AA	14.001
100-GOH-AB	11.434

Another important effect of water molecules intercalations between graphene oxide layers is hydrogen binding that reduces the total energy (compared to the non-intercalated situation). To investigate more closely the effect of intercalation of water between the plates, single-layer 100-GO and 100-GOH structures were selected, with two carbon atoms per unit cell each, and then 1 molecule of water was put in their unitcells. Then the periodic unitcell was relaxed using SIESTA. The relaxed unitcells can be seen in Fig. 25.

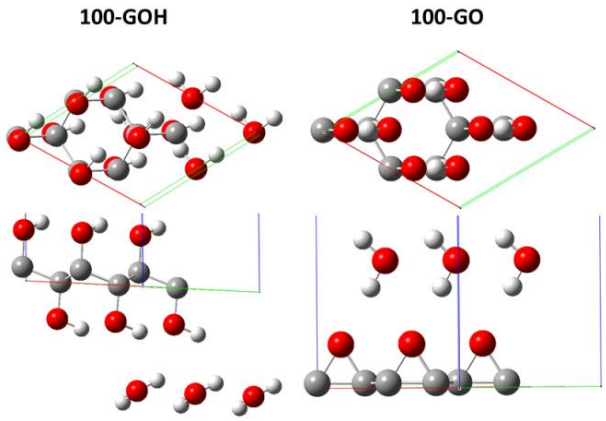

Figure 25: Relaxed structure of four water molecules adsorbed on 100-GOH (left) and 100-GO (right) structures. For 100-GO structure, oxygen atoms are located on only one side of the carbon lattice.

Due to presence of water between the layers, stability of the bilayer structure can be affected by 2 factors. First, effect of increased interlayer distance on the total energy was

calculated using UFF. After relaxation, the interlayer distance of 100-GO and 100-GOH bilayer structures were estimated to be about 4.1 and 3.3 Å respectively more than when there is no water molecule between the layers. For this increased interlayer distance, and after taking permittivity of water into account, energy of these structures increased by 0.498 and 0.449 eV for the 40 Å square sheet of the 100-GO and 100-GOH structures respectively as they can be seen in Table 13. This increased energy reduces stability of the structure. Another factor is creation of hydrogen bonds between water molecules and oxygens of graphene oxide. Binding energy of each water molecule was calculated to be 0.756 and 0.920 eV per two carbon atom unit cell for bilayer 100-GO and 100-GOH structures respectively. Taking into account that each 40 A graphene oxide layer has ~ 660 carbon atoms, the total energy of one layer of water molecules intercalated between two 40 A sheets of 100-GO and 100-GOH structures are estimated to be ~ 250 and 304 eV respectively as they can be seen in Table 13. It means the stabilizing effect of hydrogen binding between water molecules and graphene oxide by far surpasses the destabilization effect of increased interlayer disatance. Thus, due to intercalation of water, the structure is in a more stable state.

Table 13: Effect of increased interlayer distance on total enetgy and binding energy of water molecules in 40 Å square sheet.

Structure	Effect of interlayer distance on total energy of 40 Å sheet (eV)	Binding energy of water molecules in a bilayer 40 Å sheet (eV)
100-GO	0.498	250
100-GOH	0.449	304

It should be mentioned that a single-layer water molecule does not resemble continuum and simple division by water permittivity to obtain the modified energy barrier does not completely apply. However, the energy differences mentioned above are so large that this deviation from continuum would not affect the energy balance.

Comparing the result of water intercalation in between the two stacked graphene oxide layers and exfoliation of the two layers without water intercalation in the stacked state, assesed respectively by the energy balance mentioned above and calculated exfoliation rates, one observes that the route to exfoliation via water intercalation is much more feasible for stacked graphene oxide layers. This is further supported by the fact that force constants for perpendicular shifts without including the hydrogen bonding effects are larger than the corresponding force constants for parallel shifts.

3.8 Characteristics of lithium storage on graphene oxide

Li-ion batteries are rechargeable batteries with widespread applications. The material of anode or negative electrode is usually carbon. During discharge, the following reaction happens in the anode of the battery:

$$Li_xC \rightarrow x\ Li^+ + x\ e^- + C \qquad (3-5)$$

Generated electrons flow into an external circuit to do external work and Li^+ goes to cathode through electrolyte. Electrolyte needs to be ionic conductor to let Li^+ transport from and to either anode or cathode. The following reaction happens in cathode while the battery is discharging:

$$Li_{1-x}\,MO_2 + x\,Li^+ + x\,e^- \rightarrow Li\,MO_2 \qquad (3-6)$$

$LiMO_2$ or material of cathode is an Li-containing oxide and *M* is usually Co, Ni or Mn. Some polymer-based materials are also used as cathode. During discharge, Li ions come from anode through electrolyte and electrons come from external circuit. The reverse reactions happen during charging of the battery.

There have been some efforts to achieve sustainable Li-ion batteries by using renewable organic materials. For this purpose lithiation of graphene has been investigated. It has been shown that Li atoms can be adsorbed on graphene on both sides of the sheet [76] and the resulting structure has zero bandgap. Wang et al. [77] investigated use of graphene oxide with majority of epoxide groups in Li-ion battery. They used a sample of graphene oxide using exfoliation of graphite oxide and added conductive carbon black up to 15 wt% level to ensure enough conductivity of the sample. They observed oxygen in GO could react well with lithium.

3.8.1 Lithiation of Graphene Oxide and Comparing with Graphene

To investigate suitability of graphene oxide structures for Li-ion battery application and comparing it with graphene, it is needed to calculate adsorption energy of lithium on graphene oxide and diffusion energy barrier. The structures used in this part are 100-GO and 100-GOH. These structures before and after relaxation are shown in Figs. 26 and 27. Using calculated total energies of relaxed structures of lithiated graphene oxide, the relations similar to 3-1 and 3-2 were used for calculating adsorption of Li-100-GO and Li-100-GOH structures.

Adsorption energy of lithium on 100-GO is equal to +0.324 eV. Since the adsorption energy is positive, lithiation of graphene oxide is energetically favorable. Adsorption energy of Li-100-GOH is equal to -0.732 eV. The corresponding oxygen lithium distances are 1.8 and 2.1 A for lithium adsorption on 100-GO and 100-GOH structures, respectively. Because adsorption energy is negative, lithiation of 100-GOH structure is not energetically favorable and this structure is ruled out for using in Li-ion batteries. It should be mention that graphene oxide plates with high surface coverage may contain combinations of oxygen bridges and OH group. For such cases lithium adsorption happens only on oxygen bridges.

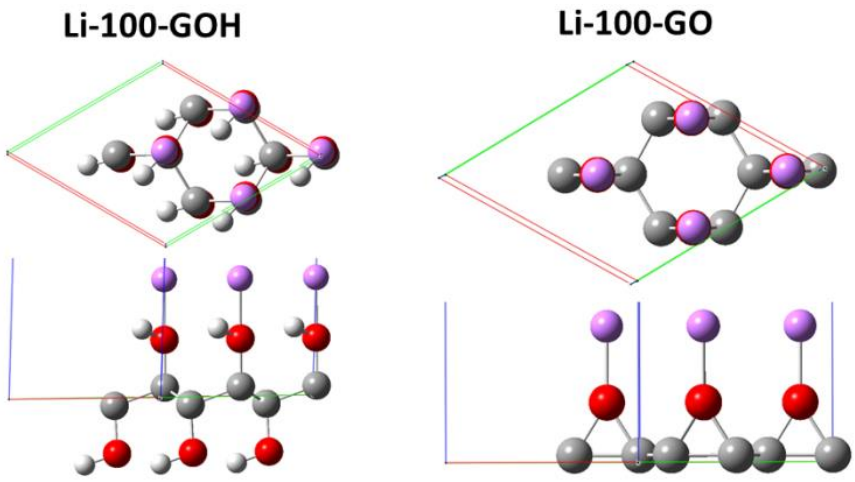

Figure 26: Two lithiated graphene oxide structures before relaxation. For 100-GO structure, oxygen atoms are located on only one side of the carbon lattice.

To compare adsorption energy of lithium in 100-GO structure with graphene, the calculations of these energies for pristine, B-doped and N-doped graphene [78] is considered. The results can be seen in Fig. 28. These energies for B-doped, pristine and

N-doped graphene are 2.71, 1.36 and 0.88 eV respectively. As it can be seen, graphene oxide structure has less energy barrier than these graphene-based structures, making delithiation process more feasible, that is an advantage of graphene oxide over graphene. It should be mentioned that higher adsorption energy causes the lithiation reaction happens faster but it makes delithiation harder. The binding energy of lithium to 100-GO structures is therefore closer to desirable values for battery functionality.

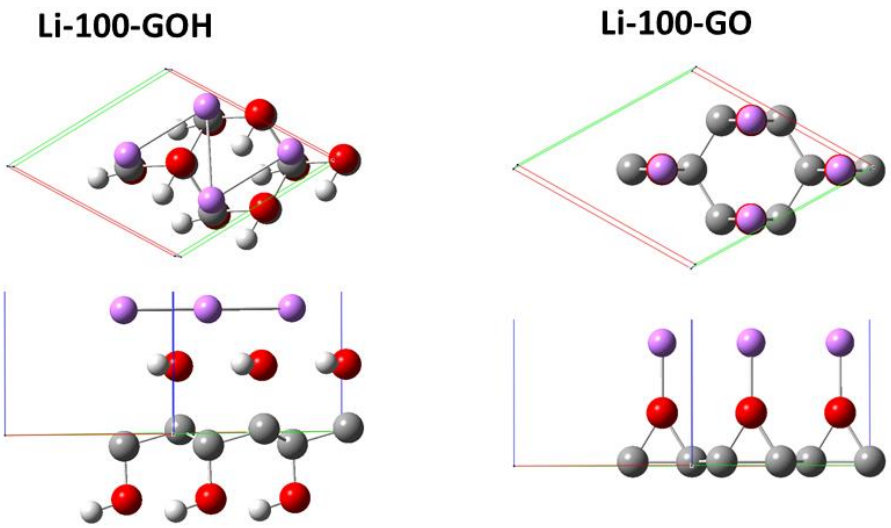

Figure 27: Two lithiated graphene oxide structures after relaxation

Another factor in comparing performance of graphene oxide and graphene in Li-ion applications is diffusion energy barrier. As it can be seen in Fig. 29, diffusion energy barrier for graphene oxide is 1.2 eV [77] while this energy for pristine, B-doped and N-doped graphene is less than 0.3 eV [78]. This means lithium atoms can move more easily

on graphene than on graphene oxide that is disadvantage of graphene oxide over graphene for battery applications.

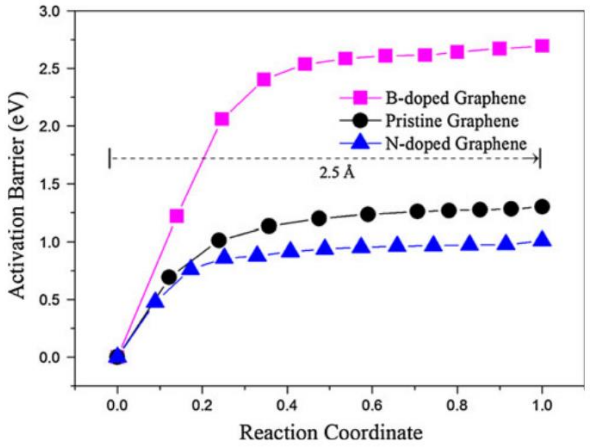

Figure 28: Energy profile for delithiation of pristine, B-doped and N-doped graphene from its original position to a place 2.5 Å above it. The energies at the far right of the curves are nearly equal to adsorption energy of lithium [78].

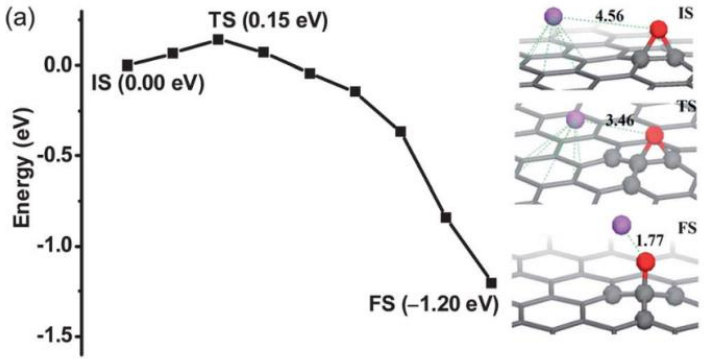

Figure 29: Diffusion energy barrier of lithium on graphene oxide [77].

4. CONCLUSION

Graphene oxide or monolayer graphite oxide as a material with organic origin is getting more attention for sustainable energy applications and its reduction to graphene is the main source of graphene production. Therefore for modeling graphene oxide, several different structures are usually needed and a large number of atoms in a unit cell must be considered to model it more accurately.

In this study, 12 different bilayer structures of graphene oxide with different oxygen coverages, AA or AB stacks and different relative positions of the bonded groups on the carbon lattice in the two layers were selected. For relaxation we used the local density approximation in density functional theory for periodic structures. There were 4 different chemical formulas (Number and types of atoms per unit cell) among these 12 structures. After first run of relaxation by SIESTA on these 12 structures, UFF calculations were used to determine the interlayer distance of minimum energy. Then, relaxed structures of the first run with calculated interlayer distance of UFF were used as input of the second run of relaxation. It was observed that output structures of the last relaxation are sometimes the same if the structures have the same chemical formula so that at the end there were only 8 different structures.

Four structures with the lowest energy in each chemical formula were chosen for calculating energy barrier of exfoliation, change in entropy and exfoliation rate. The calculations revealed that intercalation of water molecules between the layers results in a more exfoliation route compared to when there is no water molecules between the layers. Graphene oxide structures with 100% oxygen coverage were also examined for lithium

storage applications. The calculations showed that the binding energy of lithium to graphene oxide with epoxy groups is in a suitable range for lithium adsorption-desorption functionality.

Electronic band structures of different graphene oxide structures were also calculated. The results showed that structures with 50% oxygen coverage are electrical conductors but adding more epoxy or hydroxyl groups to graphene oxide opens the bandgap, making them an insulator.

REFERENCES

[1] H. P. Boehm, A. Clauss, G. O. Fischer and U. Hofmann, Z. Naturforsch., B: Anorg. Chem. Org. Chem. Biochem. Biophys. Biol., 1962, 17, 150–153.

[2] S. Stankovich, D. A. Dikin, R. D. Piner, K. A. Kohlhaas, A. Kleinhammes, Y. Jia, Y. Wu, S. T. Nguyen, R. S. Ruoff, Carbon 2007, 45, 1558.

[3] S. Stankovich, D. A. Dikin, G. H. B. Dommett, K. M. Kohlhaas, E. J. Zimney, E. A. Stach, R. D. Piner, S. T. Nguyen, R. S. Ruoff, Nature 2006, 442, 282.

[4] A. Lerf, H. He, M. Forster, J. Klinowski, J. Phys. Chem. B, 1998, 102, 4477.

[5] H. He, J. Klinowski, M. Forster, A. Lerf, Chem. Phys. Lett. 1998, 287, 53.

[6] D. R. Dreyer, S. Park, C. W. Bielawski, R. S. Ruoff, Chem. Soc. Rev. 2010, 39, 228.

[7] D. A. Dikin, S. Stankovich, E. J. Zimney, R. D. Piner, G. H. B. Dommett, G. Evmenenko, S. T. Nguyen, R. S. Ruoff, Nature 2007, 448, 457–460.

[8] Z. Q. Wei, D. E. Barlow, P. E. Sheehan, Nano Lett. 2008, 8, 3141–3145.

[9] D. R. Dreyer, S. Park, C. W. Bielawski, R. S. Ruoff, Chem. Soc. Rev., 2010, 39, 228.

[10] Tama´s Szabo´, Otto´ Berkesi, Pe´ter Forgo´, Katalin Josepovits, Yiannis Sanakis, X Dimitris Petridis, X and Imre De´ka´ny, Chem. Mater., 2006, 18, 2740-2749.

[11] H. He, T. Riedl, A. Lerf, J. Klinowski, J. Phys. Chem., 1996, 100, 19954–19958.

[12] Wilson NR, Pandey PA, Beanland R, Young RJ, Kinloch IA, Gong L, Liu Z, Suenaga K, Rourke JP, York SJ, Sloan J, 2009, ACS Nano, 3:2547.

[13] Hualan Wang, Qingli Hao, Xujie Yang, Lude Lu, Xin Wang, Electrochemistry Communications, 11, 2009, 1158–1161.

[14] Yujun Song, Konggang Qu, Chao Zhao, Jinsong Ren, Xiaogang Qu, Adv. Mater. 2010, 22, 2206–2210.

[15] A. Kumar, C. Zhou, ACS Nano 2010, 4, 11–14.

[16] D. S. Hecht, L. Hu, G. Irvin, Adv. Mater. 2011, 23, 1482–1513.

[17] F. Bonaccorso, Z. Sun, T. Hasan, A. C. Ferrari, Nat. Photonics 2010, 4, 611–622.

[18] Z. Y. Yin, S. X. Wu, X. Z. Zhou, X. Huang, Q. C. Zhang, F. Boey, H. Zhang, Small 2010, 6, 307– 312.

[19] X. Huang, Z. Zeng, Z. Fan, J. Liu, H. Zhang, Adv. Mater. 2012, DOI:10.1002/adma.201201587.

[20] Y. Wang, X. H. Chen, Y. L. Zhong, F. R. Zhu, K. P. Loh, Appl. Phys. Lett. 2009, 95, 063302.

[21] G. Eda, Y. Y. Lin, S. Miller, C. W. Chen, W. F. Su, M. Chhowalla, Appl. Phys. Lett. 2008, 92, 233305.

[22] J. Wu, H. A. Becerril, Z. Bao, Z. Liu, Y. Chen, P. Peumans, Appl. Phys. Lett. 2008, 92, 263302.

[23] L. G. D. Arco, Y. Zhang, C. W. Schlenker, K. Ryu, M. E. Thompson, C. Zhou, ACS Nano 2010, 4, 2865–2873.

[24] V. C. Tung, M. J. Allen, Y. Yang, R. B. Kaner, Nat. Nanotechnol. 2008, 4, 25–29.

[25] G. Eda, G. Fanchini, M. Chhowalla, Nat. Nanotechnol. 2008, 3, 270–274.

[26] X. Huang, X. Y. Qi, F. Boey, H. Zhang, Chem. Soc. Rev. 2012, 41, 666–686.

[27] X. Huang, Z. Y. Yin, S. X. Wu, X. Y. Qi, Q. Y. He, Q. C. Zhang, Q. Y. Yan, F. Boey, H. Zhang, Small 2011, 7, 1876–1902.

[28] Kymakis, E., Savva, K., Stylianakis, M. M., Fotakis, C. and Stratakis, E. 2013, Adv. Funct. Mater. doi: 10.1002/adfm.201202713

[29] Y. Zhou, Q. L. Bao, B. Varghese, L. A. L. Tang, C. K. Tan, C. H. Sow, K. P. Loh, Adv. Mater. 2010, 22, 67–71.

[30] Y. L. Zhang, Q. D. Chen, H. Xia, H. B. Sun, Nano Today 2010, 5, 435-448.

[31] M. F. El-Kady, V. Strong, S. Dubin, R. B. Kaner, Science 2012, 353, 1326.

[32] W. Gao, N. Singh, L. Song, Z. Liu, A. L. M. Reddy, L. Ci, R. Vajtai, Q. Zhang, B. Wei, P. M. Ajayan, Nat. Nanotechnol. 2011, 6, 496.

[33] S. H. Ko, H. L. Pan, C. P. Grigoropoulos, C. K. Luscombe, J. M. J. Frechet, D. Poulikakos, Nanotechnology 2007,18 ,345202.

[34] Zhu X. J., Guo Z. P., Zhang, P., Du, G. D., Zeng, R., Chen Z. X., Li S., Liu H. K., J. Mater. Chem. 2009, 19, 8360–8365.

[35] Lee S. H., Kim Y. H., Deshpande R., Parilla P. A., Whitney E., Gillaspie D. T., Jones K.M., Mahan A. H., Zhang S. B. Dillon, Adv. Mater. 2008, 20, 3627–3632.

[36] Arico A. S., Bruce P., Scrosati B., Tarascon J. M., Van Schalkwijk W, Nat. Mater. 2005, 4, 366–377.

[37] Pushparaj V. L., Shaijumon M. M., Kumar A., Murugesan S., Ci L., Vajtai R., Linhardt R. J., Nalamasu O., Ajayan P. M., Nanocomposite Paper. Proc. Natl. Acad. Sci. U. S. A. 2007, 104, 13574–13577.

[38] Wang H., Cui L.-F., Yang Y., Sanchez Casalongue H., Robinson J. T., Liang Y., Cui Y., Dai H., J. Am. Chem. Soc. 2010, 132, 13978–13980.

[39] Paek S. M., Yoo E., Honma I, Nano Lett. 2009, 9, 72–75.

[40] Zhu X, Zhu Y, Murali S, Stoller MD, Ruoff RS. ACS Nano. 2011 Apr 26, 5(4):3333-8. doi: 10.1021/nn200493r. Epub, 2011, Mar 31.

[41] A. Ambrosi, A. Bonanni, Z. Sofer, J.S. Cross, M. Pumera, Chem. Eur. J., 17, 2011, 10763.

[42] Yanwu Zhu, Shanthi Murali, Weiwei Cai, Xuesong Li, Ji Won Suk, Jeffrey R. Potts, and Rodney S. Ruoff, Adv. Mater., 2010, 22, 3906–3924.

[43] M. Wissler, J. Power Sources, 2006, 156, 142–150.

[44] Zhengxia Xu, Hanyang Gao, Hu Guoxin, Carbon, 49, 2011, 4731–4738.

[45] S. Stankovich, D. A. Dikin, R. D. Piner, K. A. Kohlhaas, A. Kleinhammes, Y. Jia, Y. Wu, S. T. Nguyen, R. S. Ruoff, Carbon 2007, 45, 1558.

[46] H. C. Schniepp, J. L. Li, M. J. McAllister, H. Sai, M. Herrera-Alonso, D. H. Adamson, R. K. Prud'homme, R. Car, D. A. Saville, I. A. Aksay, J. Phys. Chem. B, 2006, 110, 8535.

[47] M. J. McAllister, J. L. Li, D. H. Adamson, H. C. Schniepp, A. A. Abdala, J. Liu, M. Herrera-Alonso, D. L. Milius, R. Car, R. K. Prud'homme, I. A. Aksay, Chem. Mater., 2007, 19, 4396.

[48] M. A. Worsley, P. J. Pauzauskie, T. Y. Olson, J. Biener, J. H. Satcher, T. F. Baumann, J. Am. Chem. Soc., 2010, 132, 14067.

[49] H. A. Becerril, J. Mao, Z. Liu, R. M. Stoltenberg, Z. Bao and Y. Chen, ACS Nano, 2008, 2, 463–470.

[50] J. I. Paredes, S. Villar-Rodil, A. Martinez-Alonso and J. M. D. Tascon, Langmuir, 2008, 24, 10560–10564.

[51] I. Jung, M. Vaupel, M. Pelton, R. Piner, D. A. Dikin, S. Stankovich, J. An, R. S. Ruoff, J. Phys. Chem. C, 2008, 112, 8499.

[52] A. Buchsteiner, A. Lerf, J. Pieper, J. Phys. Chem., B 2006, 110, 22328.

[53] H.-K. Jeong, Y. P. Lee, M. H. Jin, E. S. Kim, J. J. Bae, Y. H. Lee, Chem. Phys. Lett., 2009, 470, 255.

[54] A. Nourbakhsh, M. Cantoro, T. Vosch, G. Pourtois, F. Clemente, M. H. van der Veen, J. Hofkens, M. M. Heyns, S. De Gendt, and B. F. Sels, Nanotechnology 21, 435203 (2010).

[55] J. Ito, J. Nakamura, and A. Natori, J. Appl. Phys. 103, 113712 (2008).

[56] Haiming Huang, Zhibing Li, Juncong She, and Weiliang Wang, J. Appl. Phys. 111, 054317 (2012).

[57] M. C. Payne, M. P. Teter, D. C. Allan, T. A. Arias, J. D. Joannopoulous, Reviews of Modern Physics, Vol. 64, No. 4, October 1992.

[58] Alan Hinchliffe, "Molecular Modeling for Beginners", Wiley Publications, 2008.

[59] Hohenberg P., Kohn, W, Phys. Rev., 1964, 136, B864.

[60] Kohn, W., Sham, L.J., Phys. Rev. 1965, 140, A1133.

[61] J. P. Perdew and Y. Wang Phys. Rev. B, 1986, Volume 33, Number 12, 8800-8802.

[62] A. K. Rappi, C. J. Casewit, K. S. Colwell, W. A. Goddard, W. M. Skid, J. Am. Chem. Soc. 1992, 114, 10024-10039.

[63] D. A. McQuarrie and J. D. Simon, "Physical Chemistry, A Molecular Approach", University Science Books, 1997.

[64] Van P. Carey, "Statistical Thermodynamics and Microscale Thermophysics", Cambridge University Press, 1999.

[65] C. R. Knick, "Modeling the Exfoliation Rate of Graphene Nanoplatelet Production and Application for Hydrogen Storage", 2012, Wright State University, http://etd.ohiolink.edu/send-pdf.cgi/Knick%20Cory.pdf?wright1347767528.

[66] P.Y. Yu, M. Cardona, "Fundamentals of Semiconductors, Graduate Texts in Physics", 4th ed., Springer-Verlag Berlin Heidelberg 2010.

[67] Charles kittle, "Introduction to solid State Physics", John Wiley &Sons, Inc, Eighth Edition, 2005.

[68] P. Ordejoń, E. Artacho, J. Soler, Phys. Rev. B, 1996, 53, R10441−R10444.

[69] José M. Soler, Emilio Artacho, Julian D. Gale, Alberto García, Javier Junquera, Pablo Ordejón, and Daniel Sánchez-Portal, J. Phys.: Condens. Matter, 2002, 14, 2745.

[70] M. J. Frisch, G. W. Trucks, H. B. Schlegel, G. E. Scuseria, M. A. Robb, J. R. Cheeseman, G. Scalmani, V. Barone, B. Mennucci, G. A. Petersson, H. Nakatsuji, M. Caricato, X. Li, H. P. Hratchian, A. F. Izmaylov, J. Bloino, G. Zheng, J. L. Sonnenberg, M. Hada, M. Ehara, K. Toyota, R. Fukuda, J. Hasegawa, M. Ishida, T. Nakajima, Y. Honda, O. Kitao, H. Nakai, T. Vreven, J. A. Montgomery, Jr., J. E. Peralta, F. Ogliaro, M. Bearpark, J. J. Heyd, E. Brothers, K. N. Kudin, V. N. Staroverov, R. Kobayashi, J. Normand, K. Raghavachari, A. Rendell, J. C. Burant, S. S. Iyengar, J. Tomasi, M. Cossi, N. Rega, J. M. Millam, M. Klene, J. E. Knox, J. B. Cross, V. Bakken, C. Adamo, J. Jaramillo, R. Gomperts, R. E. Stratmann, O. Yazyev, A. J. Austin, R. Cammi, C. Pomelli, J. W. Ochterski, R. L. Martin, K. Morokuma, V. G. Zakrzewski, G. A. Voth, P. Salvador, J. J. Dannenberg, S. Dapprich, A. D. Daniels, Ö. Farkas, J. B. Foresman, J. V. Ortiz, J. Cioslowski, and D. J. Fox, "Gaussain 09." Gaussain Inc, Wallingford, CT, 2009.

[71] W. Liu et al. / Journal of Physics and Chemistry of Solids 72 (2011) 299–306.

[72] L. Wirtz, A. Rubio / Solid State Communications 131 (2004) 141–152.

[73] T. H. Osborn, A. A. Farajian, J. Phys. Chem. C 2012, 116, 22916−22920.

[74] T. H. Osborn, A. A. Farajian, O. V. Pupysheva, R. S. Aga, L.C. Lew Yan Voon, Chemical Physics Letters, 511, 2011, 101–105.

[75] K. K. Paulla, A. A. Farajian, J. Phys.: Condens. Matter, 25, 2013, 115303.

[76] Yang, C.-K. Appl. Phys. Lett. 2009, 94, 163115.

[77] Da-Wei Wang, Chenghua Sun, Guangmin Zhou, Feng Li, Lei Wen, Bogdan C. Donose, Gao Qing (Max) Lu, Hui-Ming Cheng and Ian R. Gentle, J. Mater. Chem. A, 2013, 1, 3607–3612.

[78] D. H. Wu, Y. F. Li, Z. Zhou, Theor Chem Acc (2011) 130, 209–213.